



UNIVERSITY OF LEEDS

This is a repository copy of *Experimental investigation on transient characteristics of a dual compensation chamber loop heat pipe subjected to acceleration forces*.

White Rose Research Online URL for this paper:
<http://eprints.whiterose.ac.uk/123655/>

Version: Accepted Version

Article:

Xie, Y, Zhou, Y, Wen, D et al. (3 more authors) (2018) Experimental investigation on transient characteristics of a dual compensation chamber loop heat pipe subjected to acceleration forces. *Applied Thermal Engineering*, 130. pp. 169-184. ISSN 1359-4311

<https://doi.org/10.1016/j.applthermaleng.2017.11.014>

© 2017 Elsevier Ltd. All rights reserved. This manuscript version is made available under the CC-BY-NC-ND 4.0 license <http://creativecommons.org/licenses/by-nc-nd/4.0/>

Reuse

This article is distributed under the terms of the Creative Commons Attribution-NonCommercial-NoDerivs (CC BY-NC-ND) licence. This licence only allows you to download this work and share it with others as long as you credit the authors, but you can't change the article in any way or use it commercially. More information and the full terms of the licence here: <https://creativecommons.org/licenses/>

Takedown

If you consider content in White Rose Research Online to be in breach of UK law, please notify us by emailing eprints@whiterose.ac.uk including the URL of the record and the reason for the withdrawal request.



eprints@whiterose.ac.uk
<https://eprints.whiterose.ac.uk/>

Accepted Manuscript

Experimental investigation on transient characteristics of a dual compensation chamber loop heat pipe subjected to acceleration forces

Yongqi Xie, Yang Zhou, Dongsheng Wen, Hongwei Wu, George Haritos, Hongxing Zhang

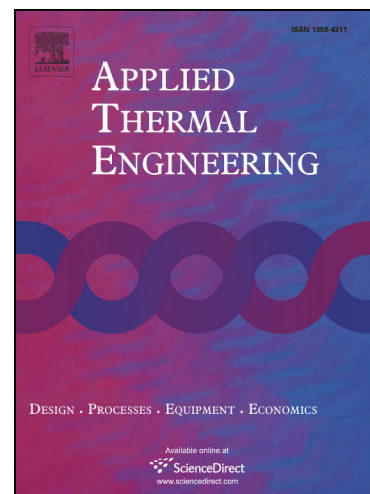
PII: S1359-4311(17)34043-7
DOI: <https://doi.org/10.1016/j.applthermaleng.2017.11.014>
Reference: ATE 11384

To appear in: *Applied Thermal Engineering*

Received Date: 14 June 2017
Revised Date: 21 October 2017
Accepted Date: 3 November 2017

Please cite this article as: Y. Xie, Y. Zhou, D. Wen, H. Wu, G. Haritos, H. Zhang, Experimental investigation on transient characteristics of a dual compensation chamber loop heat pipe subjected to acceleration forces, *Applied Thermal Engineering* (2017), doi: <https://doi.org/10.1016/j.applthermaleng.2017.11.014>

This is a PDF file of an unedited manuscript that has been accepted for publication. As a service to our customers we are providing this early version of the manuscript. The manuscript will undergo copyediting, typesetting, and review of the resulting proof before it is published in its final form. Please note that during the production process errors may be discovered which could affect the content, and all legal disclaimers that apply to the journal pertain.



Experimental investigation on transient characteristics of a dual compensation chamber loop heat pipe subjected to acceleration forces

**Yongqi Xie^{a,*}, Yang Zhou^a, Dongsheng Wen^b,
Hongwei Wu^{c,**}, George Haritos^c, Hongxing Zhang^d**

^aSchool of Aeronautic Science and Engineering, Beihang University, Beijing, 100191, China

^bSchool of Chemical and Process Engineering, University of Leeds, Leeds, LS2 9JT, United Kingdom

^cSchool of Engineering and Technology, University of Hertfordshire, Hatfield, AL10 9AB, United Kingdom

^dBeijing Key Laboratory of Space Thermal Control Technology, China Academy of Space Technology, Beijing, 100094, China

*Corresponding author: Tel: +86(10) 8233 8081, Fax.: +86(10) 8233 8952, E-mail: xyq@buaa.edu.cn

**Corresponding author: Tel.: +44(0)1707 284265, Fax.: +44(0)1707 285086, E-mail: h.wu6@herts.ac.uk

Abstract: In this article, an experimental study has been conducted to provide better understanding of the transient characteristics of a dual compensation chamber loop heat pipe (DCCLHP) subjected to the acceleration force. A new acceleration test rig was set up to provide the acceleration up to 11 g with three different directions. The heat load on the evaporator ranging from 25 W to 300 W was applied with the acceleration force simultaneously. Experimental results indicated that the DCCLHP could start up at a small heat load of 25 W and the startup behavior was different under acceleration direction conditions because of the vapor-liquid distribution change in the evaporator and compensation chambers (CCs). Under the current operating conditions, the effect of acceleration force was significant to the operating performance at small heat loads whereas was weak at large heat loads. Experimental results also clearly showed that both acceleration magnitude and direction can alter the operating mode. What's more, it was found that temperature oscillation, reverse flow and evaporation in the evaporator core phenomena occurred under acceleration conditions.

Keywords: Loop heat pipe; Dual compensation chambers; Startup behavior; Operating characteristics; Acceleration force; Electronic device cooling

Nomenclature

A	Section area, m^2
c	Specific heat capacity, $J/(kg \cdot K)$
g	Gravitational acceleration, $9.81 m/s^2$
G	Thermal conductance, W/k
I	Output current, A
L	Distance, m
m	Mass flow rate, kg/s
Q	Heat load, W
R	Physical quantity
T	Temperature, K
U	Output voltage, V
ΔT	Temperature difference, K
x	Measured variable
λ	Thermal conductivity, $W/(m \cdot K)$

Acronyms

CC	Compensation chamber
CCM	Constant conductance mode
DCCLHP	Dual compensation chamber loop heat pipe
LHP	Loop heat pipe
RTD	Resistance temperature detector
VCM	Variable conductance mode

Subscripts

cp	Cold plate
cw	Cooling water
e	Evaporator
in	At inlet
loss	heat loss
out	At outlet
vd	Voltage drop loss

1. Introduction

With the ever-increasing number of on-board electronic devices, the power level and the component integrated density become larger and larger. It is recognized that the localized heat flux of the component can be up to 100 W/cm^2 . It is, therefore, imperative to develop new techniques to remove the heat dissipation from the avionics since the capability of the typical cooling system is insufficient. Nowadays, among cooling techniques for electronic devices, loop heat pipes (LHPs) are considered as one of the most attractive ways to achieve high efficiency of heat transfer [1, 2].

LHPs utilize the vapor-liquid phase change of the working fluid to transport the heat between the evaporator and the condenser. The circulation of the fluid is driven by the capillary forces developed in the porous wicks. The advantages of the flexibility, temperature control and heat transport capability can make LHPs extend to the applications of terrestrial surroundings, aircraft, submarine and high-speed railway [3-6]. Over the past two decades, a large number of experimental, theoretical and numerical simulation studies on LHPs have been reported to provide useful data to comprehensively understand the physical mechanisms under various operating conditions and to optimize their design [7-10].

In terrestrial gravity environment, the relative position of different components will significantly influence the liquid-vapor distribution and bubble movement in the loop due to the effect of the gravity, which induces different startup behaviors and steady-state operating performances of the LHP [11, 12]. Compared to conventional LHP with a single compensation chamber (CC), the dual compensation chamber loop heat pipe (DCCLHP) was developed by configuring two CCs on the two ends of the evaporator to achieve the liquid supply for the primary wick under any orientation in terrestrial gravity.

It appears from the previous investigations that there are quite few reports on the operating performance of DCCLHP. Gerhart and Gluck [13, 14] designed a DCCLHP and verified that it could work successfully at different orientations. Their experimental results showed that the heat transfer coefficient and operating temperature were evidently different in different evaporator and CCs orientations. Wolf and Bienert [15] investigated the effect of the relative elevation of the evaporator and condenser on the temperature control characteristics of the conventional LHP and DCCLHP. It was found that the operating temperature increased as the

evaporator was elevated above the condenser. Long and Ochterbeck [16] experimentally studied the influence of the transient cyclic heat loads and orientations on the performance of a DCCLHP. They found that the startup temperature overshoot augmented with the increase of the tilt of evaporator and it had a similar performance under both constant heat load and cyclic heat load with the frequency being more than 0.1 Hz. Lin et al. [17] also designed a DCCLHP and confirmed the normal operating at any orientations. However, the operating performance was different under different orientation conditions. Bai et al. [18] experimentally studied the startup behavior for a DCCLHP with insufficient inventory and found that it could still start up at 5 W but the temperature overshoot sometimes was large. They considered that the different startup behaviors resulted from the variation of the liquid-vapor distribution and the heat leak from the evaporator to the CCs. In addition, they also investigated the temperature hysteresis, reverse flow and temperature oscillation. Lin et al. [19] carried out visual observations of the flow inside the DCCLHP and studied the start-up behavior, operating characteristics and instability. They presented detailed analyses to give insight into the operating mechanism based on the observations. Chang et al. [20] designed a DCCLHP with the visualization of CCs for the aircraft anti-icing system and carried out the experimental investigation on the thermal performance. They found that the DCCLHP could start up successfully with the heat loads from 10 W to 180 W. The angle of attack could affect the operating temperature significantly and cause temperature oscillations of the whole system.

However, the on-board electronic devices always suffer from a variety of acceleration forces when the fighter aircraft maneuvers and combats. The effect of the acceleration forces will change the performance of the cooling devices. For instance, the LHP could not start up or reach a steady state because the liquid working fluid wasn't able to sufficiently wet the capillary wick under such an acceleration field. Currently, there are only a few literatures which present the operating characteristics of the conventional LHP and DCCLHP. For the startup behavior and operation performance of a miniature aluminum-ammonia LHP in elevated acceleration environment, the impact of varying heat load, acceleration magnitude (from 0 g to 4.8 g) and direction was experimentally studied by Ku et al. [21, 22]. Their results depicted that the LHP could normally start up but temperature fluctuation happened under some acceleration conditions. Fleming et al. [23] experimentally investigated the effect of

different evaporator heat inputs (from 100 to 600 W) and radial accelerations (from 0 to 10 g) on the performance of a titanium-water LHP. It was found that dry-out conditions happened more readily at from 100 to 400 W and the reprime could be obtained after an acceleration event. The radial acceleration had little effect on the evaporative heat transfer coefficient and thermal resistance of the LHP. But the evaporator wall superheat was higher at steady state elevated accelerations comparing with 0 g. Yerkes et al. [24] carried out experimental studies on the transient operating characteristics of a titanium-water LHP under combined constant heat load and steady-periodic acceleration fields. Radial acceleration peak-to-peak values and frequency of the sine wave ranged from 0.5 g to 10 g and 0.01 Hz to 0.1 Hz, respectively. The heat load ranged from 300 W to 600 W. The results showed that the less detrimental influence there was on the LHP performance under the effect of higher acceleration frequencies and peak-to-peak amplitudes. Conversely, decreased acceleration frequency and increased peak-to-peak amplitude appear to have a greater detrimental impact on the LHP performance. Later on, the transient operating performance of a titanium-water LHP subjected to a phase-coupled evaporator heat input and acceleration field was discussed [25]. Both evaporator heat inputs (from 100 W to 700 W) and radial accelerations (from 3 g to 10 g) were generated as periodic sine wave at the frequency of 0.05 Hz. Their phase angles were set to 0° , 180° and 270° . It was found that the phase angle and condenser temperature could affect the time of LHP operating failure. This was partially due to the natural frequency of the fluid motion inside the condenser, which was effected by the induced forces resulting from the driving frequency of the acceleration coupled to the frequency of the heat input. Xie et al. [26] conducted experimentally investigation on the operating performance of a DCCLHP under terrestrial gravity and elevated acceleration conditions. The effect of the acceleration could be regarded either as an additive heat load or as a cold load. The transition of the operation mode was the function of the acceleration direction, magnitude and heat load.

To the best knowledge of the authors, there are no detailed data available in the open literatures on the effect of the acceleration forces on the operating characteristics of the DCCLHP. Hence, the objective of the present study is to provide a comprehensive experimental data exploring the transient operating performance of a DCCLHP subjected to variable heat loads and radial acceleration forces. In the current study, the evaporator heat load

and acceleration force are applied at the same time. Three different directional acceleration configurations at different acceleration magnitudes (up to 11g) are taken into account.

2. Experimental apparatus

In the current work, an experimental test rig that is used to investigate the transient operating performance of a DCCLHP subjected to acceleration forces was constructed at the Reliability and Environmental Engineering Laboratory at Beihang University, Beijing, China.

2.1 Experimental setup

The diagram of the experimental system is schematically shown in Fig. 1, which mainly consists of acceleration simulating and control subsystem, water cooling circulation subsystem, data acquisition and control subsystem as well as test section. The main components of the water cooling circulation subsystem include a gear pump, mass flow meter (DMF-1-2), thermostatic water tank, plate heat exchanger and cold plate. The thermostatic water tank kept the cooling water at 19 °C. The gear pump drove the cooling water circulating in the loop, which was regulated by a variable-frequency driver. Accurate flow measurement was accomplished by the mass flow meter based on Coriolis force with an accuracy of $\pm 0.5\%$. The cooling water absorbed the heat inside the aluminum cold plate (type 6061) and then entered the plate heat exchanger, in which it was cooled to a low temperature. Then the cooled water recycled back to the thermostatic water tank.

The data acquisition and control subsystem is mainly composed of a computer, data acquisition instrument (Agilent 34970A), resistance temperature detectors (RTDs) Pt100, electric resistance heater and precision DC power supply. The flexible polyimide film electric resistance heater was adhesively attached to the outer surface of the evaporator to apply the heat load. The range of 0-400 W can be adjusted by both altering the output voltage and current of the DC power supply (DH1716A-13) ranged from 0 to 250 V and from 0 to 5 A, respectively. The temperatures at all test points and the mass flow rate were recorded by the Agilent 34970A and saved in a remote computer located in the control room.

In the acceleration simulating and control subsystem, the acceleration force was created by spinning clockwise of the rotary arm of the centrifuge, which was driven by an electric motor. When the centrifuge operated, the radial acceleration up to 11g could be generated at the end of the rotary arm. The continuous operation for no more than an hour was required because of

safety concerns. The acceleration controller could regulate the rotational velocity of the centrifuge with an accuracy of $\pm 5\%$ of the given value. The liquid collecting rings and the electric slip rings installed in the centrifuge axis well linked up the stationary and rotational parts of the cooling water tubes, signal wires and electric wires for heating, respectively. They kept the liquid flow and the electric current working properly. A photo of the centrifuge and the test section mounted on the rotary arm was shown in Fig. 2.

In the current work, a stainless steel-ammonia DCCLHP with insufficient fluid inventory, which means the evaporator core could not be filled fully with liquid under all conditions, was manufactured in the China Academy of Space Technology. Fig. 3 illustrates a picture of the experimental DCCLHP and the detailed construction of the evaporator and the CCs. The outline size of the DCCLHP is 565 mm \times 469 mm \times 25 mm. A primary nickel wick with a pore radius of 1.5 μ m was housed in the evaporator envelope. In order to route the gas and vapor bubbles out of the evaporator core at any orientation, the bayonet was present and extended to the middle point of the evaporator core. The liquid and vapor transport lines as well as condenser line were all stainless steel smooth-walled tubes with an outer diameter of 3.0 mm. Table 1 shows a summary of the major design parameters of the experimental DCCLHP. The condenser line was welded to several cooling copper fins which were mounted on the top side of the cold plate with thermal conductive grease. All the components of the DCCLHP were wrapped with insulation materials and installed in a stainless steel enclosure, which was crammed with glass wool for thermal insulation.

Non-uniform radial acceleration forces for the whole enclosure were induced when the test section assembly was mounted on the end of the rotary arm. In order to meet the requirement of GB/T 2423.15, the acceleration magnitude should range from 90% to 130% compared to the value at the center over the test section. This could be accomplished by changing the setting value of the rotating radius of the centrifuge.

In the current work, sixteen RTDs were used to monitor the temperature profile in the experiment. Fig. 4 schematically presents the positions of the RTDs along the loop, which was placed horizontally on the rotary arm. RTD1 and RTD2 were attached on the top and bottom of the CC1 outer surface, respectively. RTD3, RTD4 and RTD5 were located on the evaporator. RTD 6 and RTD7 were attached on the top and bottom of the CC2 outer surface, respectively.

The cooling water temperatures at the inlet and outlet of the cold plate were measured by directly submersed RTD14 and RTD15, respectively. RTD16 was used to monitor the ambient temperature.

2.2 Calibration and validation

Prior to the formal experiment, calibrations of the RTDs were carried out over two temperature ranges on the basis of the estimated operating temperature. During the calibration, a constant-temperature bath was used to obtain the required temperature range. A standard platinum RTD with a resolution of ± 0.01 °C was utilized to compare the temperatures from the sixteen RTDs. When the bath reached a steady state at a given temperature, sixteen readings were sampled and the bath temperature was changed. Both cooling water temperatures at the inlet and outlet of the cold plate, as well as ambient temperature were calibrated in the range of 12 to 30 °C in 2 °C intervals. The other RTDs located on the loop were calibrated over the whole range of 12 to 60 °C in 2 °C intervals. In both estimated temperature ranges, temperature increment from the lowest to the highest value and decrement from the highest to the lowest value were conducted, respectively. The average reading at a given set-point temperature was determined based on the achieved two groups of data.

The mass flow meter used in the cooling water loop was calibrated to calculate accurately the amount of dissipate heat from the DCCLHP. When the water in the thermostatic water tank reached a steady temperature of 20 °C, the flow in the cooling water loop was diverted to a measuring device by a three-way valve installed after the flow meter. As the time span got to a specified amount of time of 360 s, the voltage from the flow meter and the mass were recorded. The mass flow rates were in the range of $m=10$ kg/h to 50 kg/h in intervals of approximate 10kg/h. Finally, the relationship between the output voltage and the mass flow rate can be achieved.

In order to verify the validation of the experimental setup, the measurement of thermal conductivity of a pure copper bar with the diameter of 30 mm was conducted under terrestrial gravity conditions. Heat load was applied at the end of the copper bar by a circular electric resistance heater. A simple copper cold plate heat exchanger was manufactured and the other end of the bar can be embedded in a circular groove in the cold plate. The cooling water absorbed the heat transmitted from the bar. Two RTDs were located at the inlet and outlet of

the heat exchanger to monitor the change of cooling water. The other two RTDs at a distance of 60 mm were attached to the outer surface of the bar to record its temperature. In the test, the cooling water in the tank was kept at 20 °C and ambient temperature was 20.1°C. The flow rate was 3.31kg/h. The whole test section was wrapped with insulation materials to minimum heat loss from the surface to the ambient.

When a steady state reached, the thermal conductivity λ could be calculated by the Fourier's law:

$$\lambda = Q_{cw}L/AA\Delta T \quad (1)$$

where Q_{cw} is the heat extracted to the cooling water, L is the distance between two RTDs locations on the bar, ΔT is the temperature difference between two RTDs located on the bar, A is the bar section area.

Comparison with the known value from Yu [27] was made based on the obtained test data and the test relative error of the thermal conductance was 8.4%.

3. Experimental procedure and uncertainty analysis

The following presents the experimental procedure, heat loss calculation for experimental setup, test data process and uncertainty analysis.

3.1 Experimental procedure

Prior to each experiment, the test section enclosure was mounted horizontally at the proper location on the rotary arm according to the given acceleration direction. Three different directions of the acceleration, namely configuration A, B and C, were employed in the present work, as shown in Fig. 5. For the cases of configuration A and B, the axis of the evaporator and CCs was consistent with the direction of the radial acceleration. The liquid line was placed at the outer edge of the rotary arm for configuration A and at the inner edge for configuration B. For configuration C, the axis of the evaporator and CCs placed at the outer edge was perpendicular to the direction of the radial acceleration.

Firstly, the data acquisition and control subsystem and water cooling circulation subsystem were turned on in turn. The cooling water started circulating flow until the whole system reached a steady state. Then the startup time of the centrifuge was set to 30 s which was the time required for the acceleration to reached a set value. Switch on the power supply for the heater while starting the centrifuge to applying the thermal load and acceleration force at the

same time. A series of experiments were firstly carried out in terrestrial gravity to achieve the basic operating behavior of the DCCLHP. Then the effect of different magnitudes and directions of the acceleration, as well as heat loads on transient operating performance was investigated.

In the current study, six different heat loads ($Q_e=25$ W, 80 W, 150 W, 200 W, 250 W, 300 W) and five radial acceleration magnitudes ($a_r=3$ g, 5 g, 7 g, 9 g, 11 g) were taken into account. It needs to be noted that the gravity is always present in all experiments. The continuous operating time of the centrifuge could not exceed 1 hour for safety. The cooling water temperature at the inlet of the cold plate was kept from 19.8 to 20.8 °C. The surroundings temperature of the centrifuge room was maintained from 25.6 to 27.5 °C by air conditioning.

3.2 Heat loss calculation

The total power, which was the product of the voltage and current output from the precision DC power supply, consisted mainly of the following three parts. The first part was the voltage drop power loss caused by the resistance of the wires themselves. The wire length was more than 15 m between the heater and the control room, which led to non-negligible voltage drop. The power loss could be achieved by multiplying the voltage drop and the current. The second was the heat loss. Because the surface temperatures of the evaporator, CCs and transport lines were larger than the surrounding temperature in general, thermal transport from these components to the surroundings contributed to the heat loss. The third part was the heat extracted to the cooling water, which was the primary heat input on the evaporator. Therefore, the heat loss Q_{loss} could be calculated approximately by the following expressions.

$$Q_e = UI - Q_{\text{vd}} \quad (2)$$

$$Q_{\text{loss}} = Q_e - mc(T_{\text{out}} - T_{\text{in}}) \quad (3)$$

Where U and I are the voltage and current output from power supply, respectively, Q_{vd} is the voltage drop power loss, m is the mass flow rate of the cooling water, c is the specific heat capacity, T_{in} is the inlet temperature of the cold plate, T_{out} is the outlet temperature of the cold plate.

In all experiments, the maximum value Q_{loss}/Q_e was not more than 16.7%.

3.3 Uncertainty analysis

The uncertainty of the physical quantity R , which was a function of the measured variables

x_1, x_2, \dots, x_i , could be calculated by the following expression [28].

$$\frac{U(R)}{R} = \left(\sum_{i=1}^n \left(\frac{1}{R} \frac{\partial R}{\partial x_i} \delta x_i \right)^2 \right)^{1/2} \quad (4)$$

where δx_i denotes the uncertainty of the i th measured variable.

In the present work, the thermal conductance of the DCCLHP was determined by the evaporator temperature and the cold plate temperature:

$$G = Q_e / (T_e - T_{cp}) \quad (5)$$

where G is the thermal conductance, T_e is the evaporator temperature, T_{cp} is the average temperature of the cold plate, which can be calculated by Eq. (6):

$$T_{cp} = 0.5(T_{out} + T_{in}) \quad (6)$$

As taking into account the effect of the RTDs, electric wire, slip rings, junction terminal and data loggers, the accuracies of the temperature measurements were approximately ± 0.5 °C. The maximum uncertainty of the temperature was 2.6%. The maximum uncertainty of the voltage and current was 4.6% and 2.9%, respectively. As a result, the maximum uncertainty of the heat load was 5.4%. According to Eq. (5) and (6), the maximum uncertainty of the thermal conductance was approximately 10.5%.

4. Results and discussion

The following sections will address both the startup and operating characteristics of the DCCLHP as it was subjected to different acceleration directions, acceleration magnitudes and heat loads on the evaporator based on a series of experiments.

4.1 Effect of the acceleration directions

Fig. 6 illustrates the loop temperature profiles at 5 g and 25 W for configuration A, B and C. Fig. 7 schematically shows the estimated vapor-liquid distributions in the loop subjected to the acceleration force for the three configurations. During the experiment, the whole procedure could be divided into three phases: the terrestrial steady phase, the acceleration phase and the unloading phase. In the terrestrial steady phase, the DCCLHP is operated at a steady state with the effect of the cooling water. The acceleration force and the heat load are applied during the acceleration phase, whereas the acceleration force is removed in the unloading phase.

As can be seen clearly in Fig. 6, the temperature profiles of the loop under configuration A,

B and C show quite different behaviors. For the case of configuration A, the temperature varies slowly within the first 250 s, whereas a temperature peak value occurs at approximate 200 s for both configurations B and C. In Fig. 6(a), it is at 169 s that both acceleration force and heat load are applied simultaneously. The temperature of the evaporator and CC1 (RTD1 and RTD2) rises immediately when the heat load is applied to the evaporator. The RTD8 temperature at the outlet of the vapor line also steeply increases from 22.2 °C to 24.4 °C nearly at the same time. It could be explained by the fact that the evaporation occurred and the vapor existed in the evaporator grooves at the very beginning. Compared to the temperature rise of RTD4 and RTD8, the temperature for both the condenser (RTD9 and RTD10) and the liquid line inlet (RTD11) decreases approximately 1 °C. Especially for the liquid line, the temperatures of RTD12 and RTD13 show a very steep drop at 173 s. This indicates that the subcooling liquid from the condenser reaches the outlet of the vapor line and the positive fluid circulation starts. Therefore, the startup is deemed a success and the startup time is approximately 4 s.

When the acceleration force is applied, the vapor-liquid distribution is changed due to the force effect, as shown in Fig. 7(a). The liquid of the working fluid in the CC1 and evaporator core will be pushed into the CC2. As a result, the level of the liquid in the CC1 reduces to the evaporator core, but the level in the CC2 rise above it. This distribution will result in the increase of the heat leak from the evaporator to the CC1 and decrease to the CC2. Therefore, the CC1 temperature increases obviously. The CC2 temperature starts to drop until 199 s due to the returning liquid cooling. Under the effect of the acceleration force during the initial period, the liquid with lower temperature in the condenser flows through the right bends of U-shaped coils and easily enters the liquid line and goes back to the evaporator. Consequently, the temperature from RTD9 to RTD13 drops. With the increase of the condensation temperature in the condenser, the temperature from RTD9 to RTD13 rises in turn. As an equilibrium state of the loop reaches finally, the temperature of the evaporator, CC1 and CC2 are 25.2 °C, 24.8 °C and 21.7 °C, respectively.

In the unloading phase, the gravity will make the liquid in the CCs and evaporator core to be in the same level again. It is noted that the heat leak from the evaporator to CC2 increases. Therefore, the CC2 temperature shows a steep rise with the increase of the evaporator temperature. In the current work, the operating performance after unloading the acceleration

force will not be discussed here in detail.

For the case of configuration B, as demonstrated in Fig. 6(b), the evaporator temperature shows a steep rise as the heat load is supplied at 63 s. The RTD8 temperature increases approximately 0.4°C . In the meantime, the temperature of RTD9, RTD10 and RTD11 changes slightly. Nevertheless, the RTD12 and RTD13 temperature shows no obvious changes. The reason could be that the fluid flow in the external loop is driven by the acceleration force. Since the radial acceleration force is small and the tangential acceleration force will dominate during the initial period, the liquid with lower temperature in the coils of the condenser is driven to pass through the right U-shaped bends and then enters the liquid line.

However, it is almost at 69 s that the RTD8 temperature begins to decrease rapidly and the RTD13 temperature increase remarkably, as well as both RTD9 and RTD10 temperatures decrease sharply. It is noted that the RTD11 temperature increases dramatically starting from 71 s. The RTD12 temperature shows a steep rise until 83 s. The reason could be attributed to the contribution of the following coupled with Fig. 7(b). When the radial acceleration force dominates, both the vapor phase and liquid phase are redistributed in the loop due to the effect of the acceleration force. Moreover, it is likely that the evaporation occurred in the evaporator core. The liquid will be pushed from the CC2 and evaporator core into CC1 and the vapor floats into the CC2, even reversely get into the liquid line via the bayonet. As a result, the heat leak from the evaporator to the CC2 increases but decreases to the CC1. There is a slight rise for both RTD1 and RTD2 temperature and a sharp rise for both RTD6 and RTD7 temperature with almost the same value. The reverse of the vapor in the liquid line results in the increase of the RTD12 and RTD11 temperatures. The liquid from the condenser entering the vapor line leads to the drop of the RTD8 temperature.

It is found that at 139 s the RTD8 temperature shows a very steep rise from 21.0°C to 30.3°C . This demonstrates that the evaporation occurs in the evaporator grooves and the vapor arrives at the outlet of the vapor line. The RTD11 temperature decreases rapidly at the same time. Then the RTD 12 temperature drops dramatically after 141 s while the RTD13 temperature drops after 143 s. At this moment, the circulation flow forms and the DCCLHP starts up. After the evaporator temperature reaches the highest of 31.7°C at 183 s, the temperatures of the evaporator, CC2 and vapor line decrease to a constant value gradually. It is

believed that the entire loop reaches an equilibrium state at 2400 s. The temperatures of the evaporator, CC1 and CC2 at the steady state are 25.5 °C, 25.3 °C and 24.6 °C, respectively. In the unloading phase since 2800 s, the evaporator temperature drops slightly and then increases.

In addition, the RTD9 temperature increases suddenly and begins to oscillate at 1125 s. The RTD13 temperature also oscillates simultaneously but the temperatures of the RTD10, RTD11 and RTD12 show no oscillation. Furthermore, this oscillation sustains approximately 650 s and disappears. This phenomenon may not be explained clearly now but will be further studied in the future work.

According to the temperature profiles shown in Fig. 6(c), it is recognized that the temperatures of the evaporator and CCs increase as the heat load is applied at 85 s. But the temperatures of the condenser and transport lines show no apparent variations before 95 s. It is at 95 s that the RTD11 and RTD13 temperatures increase significantly. It could be the reason that the tangential acceleration force changes the vapor-liquid distributions in the loop during the initial period of the centrifuge rotating. A partial of liquid is pushed into the CC1 from the CC2 and evaporator core, where the vapor-liquid distribution is illustrated in Fig. 7(c). It could be explained by the fact that there exist bubbles in the evaporator core or the vapor occurs inside of the wick and the evaporation happens in the evaporator core prior to the vapor grooves. The vapor through the bayonet flows into the liquid line. As a result, the RTD13 temperature increases rapidly. In the condenser, the liquid could gather in the left U-shaped bends due to the effect of the tangential acceleration force. And there is no massive fluid flow into or out of the condenser. Therefore, the temperatures of the RTD8, RTD9, RTD10 and RTD11 show no obvious changes. However, the RTD8 temperature begins to drop at 101 s. It is indicated that the liquid reversely flows into the vapor line from the condenser. It is worth to note that the RTD12 temperature shows a very small change before 165 s as the RTD11 and RTD13 temperature increases significantly. The reason could be that the annular flow is formed in the liquid line due to the effect of the radial acceleration force. A thin liquid layer prevents the wall temperature from increasing until it completely evaporates to the vapor.

At 167 s, the RTD8 temperature reaches the minimum value of 22.1 °C and the RTD11 temperature gets to the maximum value of 24.8 °C. Afterwards, the RTD8 temperature increases quickly and the RTD11 temperature drops. This shows that the vapor via the vapor

line enters the condenser and then flows into the liquid line. It is at 171 s that the peak temperatures of the RTD4 and RTD13 reach 31.0 °C and 30.0 °C, respectively. According to the variation of the external loop temperatures, the DCCLHP starts up after 82 s since the heat load is applied.

After 171 s, the temperatures of the evaporator, vapor line and CCs drop gradually. But the condenser temperature increases slowly and then drops. The liquid line temperature decreases rapidly to a constant and then increases quickly. When the time is 791 s, the DCCLHP reaches a thermal equilibrium state and the final operating temperature is 23.6 °C. It is obviously different with the cases of configuration A and B that the whole loop temperatures ranges from 22.8 °C to 23.6 °C, which are higher than the sink temperature but lower than the ambient temperature. The above phenomenon can be explained as the following. Under configuration C, the effect of the acceleration force is similar to the gravity-assisted effect. After the DCCLHP starts up, the capillary pressure difference across the wick exceeds the total loop pressure drop since the effect of the acceleration force promotes the subcooling liquid returning to the evaporator. Therefore, the capillary pressure difference decreases and the relevant temperature difference also decreases in order to balance the total loop pressure drop. This reduces the heat leak, which causes the decrease of the operating temperature. Moreover, the loop pressure equilibrium does not reach if the capillary pressure difference reduces to 0 Pa. The acceleration force will drive the working fluid circulating in the loop. Consequently, a two-phase flow occurs in the vapor line and both the vapor and the liquid are saturated. It could be confirmed that the RTD8, RTD9 and RTD10 temperatures are almost equal. In addition, it is likely that the actual liquid evaporation area is reduced by the effect of the acceleration force under this configuration. This could also lead to the decrease of the evaporation temperature. In the unloading phase after 2217 s, the temperatures of the evaporator and CCs increase slightly and the RTD12 and RTD13 temperatures increase gently and then drop. The RTD10 and RTD11 temperatures decrease moderately.

Fig. 8 presents the loop temperature profiles at 250 W and 5 g under configuration A, B and C. Partial enlarged drawings are also shown in order to see clearly the temperature variations. According to the graphs shown in Fig. 8, it could be found that the RTD4 and RTD8 temperatures increase immediately as the heat load is applied for three different configurations.

This indicates that the evaporation occurs in the vapor grooves and the vapor enters the condenser. The RTD11 and RTD13 temperatures drop almost at the same time. It is believed that the DCCLHP starts up under configuration A, B and C. However, the loop is not able to reach a steady state under configuration A during the period of the centrifuge operating. The temperature oscillations occur under configuration B and a thermal equilibrium state reaches under configuration C.

For the case of configuration A shown in Fig. 8(a), when the heat load and acceleration force is applied at 57 s, the positive circulation of the working fluid starts rapidly in the loop on the basis of the loop temperature changes. The liquid in the condenser is driven into the liquid line, resulting in the temperatures of RTD11, RTD12 and RTD13 drops. The RTD9 and RTD10 temperatures near the RTD8 temperature shows that the condensing area of the condenser enlarges and the subcooling of the liquid decreases. As a result, the RTD11 and RTD13 temperatures increase sharply after 71 s and 79 s, respectively. The condenser is completely opened until the RTD11 temperature is nearly equal to the RTD10 temperature. Therefore, the vapor front advanced to the outlet of the condenser, displacing the equal volume liquid toward the CCs. The effect of the acceleration force changes the vapor-liquid distribution in the CCs, which is similar to the results that shown in Fig. 7(a) but more liquid in the CC1. The heat leak reduces from the evaporator to the CC2. Simultaneously, owing to the convection and cold bayonet inside the CC2, the CC2 temperature is less than that in CC1.

However, it is at 355 s that the temperatures of RTD11, RTD12 and RTD13 begin to decrease. This shows that the subcooling of the returning liquid increases. The RTD6 and RTD7 temperatures reduce due to the cooling effect of the returning liquid. The vapor-liquid interface moves back to a certain position before RTD10 point in the condenser. When the time is at 1703 s, the RTD10 temperature drops suddenly. It shows that the vapor-liquid interface moves back to a certain position between RTD9 and RTD10 point. The condenser is not fully used. Finally, the DCCLHP fails to reach a steady state and the maximum temperature of the evaporator is 40.6 °C.

In the unloading phase after 2815 s, the change of the vapor-liquid distribution results in the heat leak increasing from the evaporator to CC2 as the acceleration force is out of action. The CC2 temperature increases steeply. The temperatures of the evaporator, CC1 and vapor line

drop slightly and then increase slowly. But the liquid line temperatures changes a little.

Under configuration B, when the acceleration force and heat load are applied at 61 s, the RTD8 temperature increases immediately and the RTD11 temperature drops, as shown in Fig. 8(b). This indicates that the vapor occurs and enters the condenser, as well as the subcooling liquid from the condenser flows into the liquid line. It is at 67 s and 71s that the RTD11 and RTD13 temperatures begin to increase sharply, respectively. With the aid of the CC1 and CC2 temperatures, it is believed that the CC1 is almost full of the cooling liquid and the CC2 is filled with a large amount of vapor under the effect of the acceleration force. Therefore, the heat leak from the evaporator to CC1 is small whereas to CC2 is large. The RTD1 and RTD2 temperatures show a slight rise but the RTD6 and RTD7 temperatures increase rapidly.

With the input of the heat load, the loop temperatures except for CC1 begin to oscillate at a certain time after 110 s and the amplitude become larger and larger gradually. It is difficult to determine which component first starts to oscillate. Perhaps both CC2 and condenser show oscillation simultaneously. It is on the liquid line that the amplitude of the periodic temperature oscillation suddenly become larger after approximate 380 s and is larger than that of the other components. Moreover, the amplitudes of RTD11, RTD12 and RTD13 enlarge in turn. According to the periodic temperature oscillation, a persistent forward and reverse liquid flow in the liquid line does alternate as evidenced by the temperatures of the liquid line inlet (RTD11) and outlet (RTD13). The RTD11 and RTD13 temperatures oscillate between 25.7 °C and 30.2 °C, as well as 25.6 °C and 31.4 °C, respectively. The RTD11 and RTD13 temperatures oscillation has a nearly same period of 144 s. However, it is clearly seen that the RTD13 temperature oscillation pattern is not symmetric. It takes around 94 s to drop from the peak temperature to the valley, and 50 s to rise from the valley temperature to the peak. The oscillating temperature shows a similar change for the CC2, evaporator and condenser. Finally, a quasi-stable state is established where the peak and valley for the evaporator and CC2 temperatures are 35.4 °C and 34.4 °C, as well as 33.3 °C and 32.3 °C, respectively. Their temperature oscillation periods are both around 120 s. After the acceleration force is unloaded at 2020 s, the evaporator and CCs temperatures rise sharply but the liquid line temperature drops.

The underlying physical mechanism during the temperature oscillations and the interactions

among the DCCLHP various components could be explained as the following. When the RTD11 temperature begins to drop from the peak, the vapor front would go back to the condenser and recede gradually. Since additional liquid from the CCs via the bayonet is used to replenish the space left by the vapor recession, the liquid flow in the liquid line would reverse. Under this situation, the reverse liquid flows in the liquid line and the forward vapor flows in the vapor line, both are existed simultaneously. As the liquid recedes inside the condenser, the acceleration pressure head would increase. In order to balance the loop pressure, the capillary pressure difference increases which requires the CC2 temperature to rise. The loop pressure is balanced as the CC2 temperature reaches its peak value. In the meantime, the evaporator temperature also increases and reaches its peak value. Consequently, the vapor front stops receding and starts to advance. At the same time, the liquid length inside the condenser reaches its maximum as well. When the front goes forward and arrives at some point in the condenser, the RTD11 temperature falls to its valley value. As soon as the front advances, the acceleration pressure head decreased. The relevant capillary pressure difference decreases to balance the loop pressure. As a result, the CC2 temperature drops and the evaporator temperature drops following the CC2. As the front advances, the subcooling of the liquid from the condenser reduces. This results in the RTD11 temperature increases. It would reach the peak value until a certain time after the vapor-liquid front rushed out of the condenser. The front rushing out could be due to the insufficient inventory of the working fluid and the flow inertia effect as well. When the subcooling of the returning liquid could not balance the heat leak, the CC2 temperature stops falling and starts to rise. This starts the next cycle of the loop rise and fall above.

However, it is very difficult to completely explain the fluid flow and temperature oscillations. It could be the reason of the complexity and instability of the two-phase flow and heat transfer, impacted by many coupled factors such as the acceleration force, degree of subcooling, heat load and mass flow rate. It is also related to the adaptation of the CCs volume and the fluid inventory. Temperature oscillation is undesirable because of the deleterious effects on the precise temperature control in practical application. Therefore, it is extremely essential that the oscillation mechanism is further investigated.

As can be clearly seen from Fig. 8(c), the RTD8 temperature increases immediately as soon

as the head load is applied at 141 s under configuration C. The vapor reaches the outlet of the vapor line. As opposed to the RTD8, the temperatures of the condenser and liquid line drop and then increase rapidly. It is at 149 s and 153 s that the temperatures of RTD11 and RTD13 increase, respectively. Because the vapor-liquid distributions in the CCs and evaporator core caused by the acceleration force is similar to that under the terrestrial gravity, both CC1 and CC2 temperatures increase. This distribution is different with that under configuration A and B. After 207 s, the RTD11, RTD12 and RTD13 temperatures show a momentary oscillation and then decrease to a constant value. In the condenser, the RTD9 and RTD10 temperatures near the RTD6 temperature are much higher than the RTD11 temperature. This means that the vapor-liquid interface locates at some point in the condenser, and the condenser is not fully used. It is believed that the DCCLHP reaches a steady state at 2000 s. At the steady state, the evaporator temperature is approximate 36.9 °C. The RTD6 and RTD7 temperatures are 35.5 °C and 34.9 °C, respectively. Both RTD1 and RTD2 temperatures are close to 35.2 °C. After the centrifuge stops at 2770 s, the evaporator temperature reaches 37.5 °C at a steady state. The RTD6 and RTD7 temperatures are 35.5 °C and 30.3 °C, respectively. The RTD1 and RTD2 temperatures are close to 35.6 °C.

Compared the profiles shown in Fig. 6 with those in Fig. 8, it can be found that the startup behavior of the DCCLHP is susceptible to the direction of the acceleration force at a small heat load of 25 W. The evaporation inside the core and the reverse flow in the external loop could happen under configuration B and C. At a larger heat load of 250 W, the DCCLHP is able to start up quickly under different configurations. But whether the DCCLHP can reach a steady state is dependent on the acceleration direction. Moreover, the periodic temperature oscillation and reverse liquid flow occurs under configuration B.

Fig. 9 depicts the operating temperature and thermal conductance at different heat loads under three different configurations and terrestrial gravity as the acceleration magnitude is 5 g. Note that the evaporator temperature ascends continuously and the loop fails to reach a steady state during the given time for these cases of 25 W, 80 W and 150 W in terrestrial gravity as well as 150 W, 200 W and 250 W at 5 g under configuration A. The maximum value of the evaporator temperature is used instead of the steady operating temperature for the comparison.

As can be seen in Fig. 9(a), quite different behavior on the operating temperature is shown

under different configurations and terrestrial gravity as the heat load is less than 200 W, but had a small difference at a larger heat load of 300 W. The operating temperatures are 45.7 °C, 40.0 °C and 38.5 °C under terrestrial gravity when the heat load is 200 W, 250 W and 300 W, respectively. The operating temperatures at 300 W under configuration A, B and C are 37.6 °C, 38.4 °C and 39.0 °C, respectively. Under terrestrial conditions, the DCCLHP has a higher operating temperature than that under acceleration conditions. When the heat load ranged from 150 W to 300 W, there is a small difference of the operating temperature at a fixed heat load between under terrestrial gravity and under configuration A.

For configuration A at 5 g, the steady state reaches for the cases of 25 W, 80 W and 300 W and the operating temperatures are 25.2 °C, 38.6 °C and 37.6 °C, respectively. But it cannot reach in the given time as heat loads are 150 W, 200 W and 250 W. Compared with the cases in terrestrial gravity, the effect of the acceleration force promotes the DCCLHP operating under a small heat load. However, the reverse effect occurs at a moderate heat load. For the cases of configuration B and C at 5 g, the DCCLHP can reach a steady state and has a lower operating temperature. When the heat load is no more than 150 W, the operating temperature under configuration B is larger than that under configuration C. However, the opposite happens as the heat load is no less than 200 W.

In Fig. 9(b), it is seen that the thermal conductance at 5 g generally shows a trend of increase with the increase of the heat load under acceleration and terrestrial conditions. For the thermal conductance at a fixed heat load, there is a relatively large difference among various configurations and terrestrial as the heat load does not exceed 200 W, whereas a small value as the heat load is not less than 250 W. When the heat load exceeds 150 W, there is nearly the same thermal conductance at a fixed heat load under between terrestrial gravity and configuration A.

In terrestrial gravity, the condenser is not fully opened as heat load is less than 300 W. The DCCLHP operates at variable conductance mode (VCM). For configuration A, it operates at VCM at both 25 W and 80 W and at constant conductance mode (CCM) at 300 W. For configuration B, the heat loads at VCM and CCM range from 25 W to 150 W and from 200 W to 300 W, respectively. For configuration C, the thermal conductance ranges from 14.7 W/K to 21.4 W/K. It is only at 300 W that the loop operates at CCM since the condenser is fully used.

To sum up, the effect of the acceleration force changes the startup behavior and operating mode of the DCCLHP. The impact of the acceleration direction on the operating temperature is significant at small heat load (≤ 150 W) but is weak at large heat load. The effect of the acceleration direction changes the heat load range of VCM or CCM.

4.2 Effect of the acceleration magnitude

Fig. 10 shows the temperature profiles of the loop at 80 W under terrestrial gravity and under configuration A at 5 g. As can be seen from the figure, the loop temperature shows a gradual increase to its maximum value following a near steady value in terrestrial gravity. But it slowly goes up to a constant value under configuration A. Under both conditions, there is an obvious difference for the RTD6 and RTD7 temperatures of the CC2.

In Fig. 10(a), once the heat load is applied at 41 s, the RTD4 temperature augments from 24.3 °C to 25.2 °C. Almost at the same time, the RTD8 temperature ascends from 22.5 °C to 24.5 °C, which is a consequence of the vapor arrives at the outlet of the vapor line. It shows that the positive circulation flow is established coupled with the drop of the temperatures from RTD9 to RTD13 and the DCCLHP starts up. Because there is the same level of the liquid in the CCs and core, which determines their thermal link under terrestrial conditions, the RTD1 and RTD6 temperatures increase much faster than that of the RTD2 and RTD7 temperatures. From 90 s to 341 s, the temperatures of the evaporator, vapor line and CC1 remain almost unchanged. The RTD10 temperature gradually increases to 24.0 °C until 245 s. It reveals that the vapor length inside the condenser increases. It is at 369 s that the RTD10 temperature drops again, which indicates the vapor-liquid interface recedes inside the condenser. As a result, the reverse liquid flow in the liquid line occurs and the additional liquid from the CCs is fed to fill the space in the condenser left by the recession. Therefore, the RTD13 temperature rises and then drops until the positive flow starts.

After 343 s, the RTD1 and RTD4 temperatures augment again. It is at 403 s that the RTD9 temperature begins to descend, which shows the vapor-liquid interface recedes to a certain point before RTD9 point in the condenser. The condenser is not fully opened. The RTD6 and RTD7 temperatures are lower than that of the RTD1 and RTD2 due to the cooling effect of the returning liquid. Because the evaporator temperature gets to 50.8 °C at 893 s, the heat load is removed when taking the safety into consideration. Then the temperatures of the evaporator

and the CC1 decreases gradually but the RDT13 temperature increases rapidly.

For the case of configuration A, as presented in Fig. 10(b), the startup behavior is similar to the case of terrestrial gravity, as shown in Fig. 10(a) during the initial approximate 20 s when switching on the acceleration force at 79 s. Under this condition, the vapor-liquid distribution is similar to the case as shown in Fig. 7(a). Thereby, the heat leak declines from the evaporator to the CC2. In the meantime, the returning liquid with some degree of subcooling cools the fluid in the CC2. Consequently, the RTD6 and RTD7 temperatures do not ascend.

It is at 929 s that the RTD9 temperature begins to descend quickly. It shows that the vapor front recedes to some point before the RTD9 point in the condenser and the condenser is not completely used. During the period from 1705 s to 2849 s, the loop remains a thermal equilibrium state. The evaporator temperature is 38.6 °C and the CC1 and CC2 temperatures are 38.0 °C and 23.2 °C, respectively. However, it should be noted that the evaporator and the CC1 temperatures shows a rapid rise as soon as the acceleration force is unloaded at 2489 s.

The loop partial temperature evolutions at 300 W with four different accelerations of 3 g, 5 g, 7 g and 9 g under configuration B are shown in Fig. 11. Because there are similar startup behaviors for all acceleration magnitudes, only the partial enlarged drawing at 3 g during the initial period is shown for the purpose of brevity. For the case of 3 g, as the heat load is applied at 51 s, the RTD4 and RTD8 temperatures rapidly ascend. This indicates that the vapor is generated and gets to the outlet of the vapor line at larger heat load of 300 W. According to the drop of the RTD10, RTD11 and RTD13 temperatures, it is believed that the DCCLHP starts up.

As can be clearly seen from the figure, there are temperature oscillations in the loop for all acceleration magnitudes. The amplitudes of the evaporator, CC2, condenser and vapor line are smaller than that of the liquid line under each acceleration magnitude. As the acceleration magnitude is 3 g, the amplitude and period are the largest. There are small differences of the period and amplitude under 5 g, 7 g and 9 g conditions. Under all acceleration magnitudes, the loop reaches a quasi-steady state finally. The valley and peak values of the evaporator temperature at 3 g, 5 g, 7 g and 9 g are 36.9 °C and 37.6 °C, 38.0 °C and 38.4 °C, 37.5 °C and 38.0 °C, as well as 38.1 °C and 38.5 °C, respectively. The relevant periods are 28 s, 18 s, 18 s and 20 s, respectively.

Fig. 12 shows the operating temperature and thermal conductance at 150 W, 250 W and 300 W under five different accelerations of 0 g, 3 g, 5 g, 7 g and 9 g for configuration B. The maximum temperature is used at 150 W under terrestrial gravity since the loop fails to reach a steady state. The peak value of the evaporator temperature is utilized as the temperature oscillates at 250 W and 300 W under all acceleration magnitudes conditions.

It is found from Fig. 12(a) that the operating temperature is not susceptible to the acceleration magnitude under configuration B as the heat load is large. Corresponding to the case of terrestrial gravity, the effect of the acceleration force significantly reduces the operating temperature, especially at 150 W. The overall trend of the operating temperature appears enlargement with the increase of heat load under acceleration conditions. As the heat load is 150 W, the evaporator temperatures are 55.8 °C, 35.4 °C and 35.9 °C at 0g, 3g and 5g, respectively.

As can be seen in Fig. 12(b), the thermal conductance at 250 W and 300 W is obviously larger than that at 150 W under acceleration conditions. There is nearly the same value at 250 W and 300 W for a fixed acceleration magnitude. When the heat loads are 250 W and 300 W, the thermal conductance ranges from 21.4 W/K to 22.9 W/K under acceleration conditions. In addition, compared with the values at gravity terrestrial, the thermal conductance is larger under acceleration conditions.

Fig. 13 presents the partial temperature evolutions of the loop at 80 W and five different accelerations of 3 g, 5 g, 7 g, 9 g and 11 g under configuration C. As is shown in Fig. 13, there is a peak for the RTD4 curve under all acceleration magnitudes. The RTD4 temperature at 3 g is much larger than that at the other acceleration magnitudes. Temperature oscillations occur at 7 g and 9 g. The transient operating performance differs from each other and does not show an obvious regularity under different acceleration magnitudes.

For the case of 3 g, when the acceleration force and heat load are applied at 53 s, the RTD4 temperature ascends immediately and RTD8 temperature also goes up steeply. This confirms that the vapor from the grooves gets to the outlet of the vapor line. The quick successive drop of the RTD10, RTD11 and RTD13 temperature in further indicates the positive circulation flow starts and the DCCLHP starts up. For the cases from 5 g to 11 g, startup processes are similar to the case of 3 g. There is a small peak for the RTD4 temperature profile during the period

from 140 s to 170 s. Then the temperatures of RTD4, RTD1 and RTD6 gradually increase. Finally, it takes approximate 1100 s to reach the steady state. Because of the vapor-liquid distribution in the CCs is similar to that shown in Fig. 7(c), the heat leaks are almost equal from the evaporator to CC1 and CC2. Therefore, the RTD1 and RTD6 temperatures are nearly the same. It is believed that the condenser is not fully opened according to the RTD10 and RTD11 temperatures.

For the case of 5 g, after the DCCLHP starts up, there is a large peak for the RTD1, RTD4, RTD6 and RTD8 curves. It takes approximate 800 s for the loop to reach a thermal equilibrium state (the profiles do not be shown in Fig. 13). The final operating temperature is 26.7 °C. It is obviously different with the cases of 3 g that the whole loop temperatures ranges from 25.3 °C to 26.0 °C except for the evaporator temperature. It could be inferred that there is two-phase flow in the vapor line. Furthermore, the fluid in the entire condenser could be interpreted as two-phase flow. In addition, for the case of 11 g, the loop temperature distribution is similar to the case of 3 g, which ranges from 25.7 °C to 26.4 °C except from the evaporator temperature with 27.0 °C.

Under conditions of 7 g, only the RTD4 and RTD10 temperature has a slight oscillation in the loop. It takes approximate 1400 s to reach the steady state. At the steady state, the RTD10 temperature is 2.6 °C lower than the RTD9 temperature whereas is 1.7 °C higher than the RTD11 temperature. This indicates that the condenser is not completely opened. Compared with the case of 7 g, the temperature oscillation of the whole loop shows more obviously at 9 g. It takes approximate 136 s when the temperature oscillation starts after switching on the heat load. Finally, a quasi-steady state is reached at around 1600 s and the evaporator temperature is around 27.4 °C. Because the RTD11 temperature is much lower than that of the RTD9 and RTD10, it means that the subcooled liquid exists in the condenser and the condenser is completely used.

Fig. 14 depicts the operating temperature and thermal conductance at 80 W and 200 W under acceleration conditions for configuration C. As is shown in Fig. 14(a), it is found that the effect of the acceleration magnitude has a significant impact on the operating temperature under configuration C. As the acceleration is large, the operating temperature change shows a trend of decline with the increase of the acceleration magnitude. The operating temperature at large heat

load is higher than that at small heat load under acceleration conditions. Moreover, the effect of the acceleration force on the loop temperature becomes weak when the acceleration magnitude exceeds 5 g at 80 W. The operating temperatures are 32.2 °C, 26.7 °C, 28.4 °C, 27.4 °C and 27.0 °C at 3 g, 5 g, 7 g, 9 g and 11 g, respectively. When the heat load is 200 W, it is more than 7 g that the effect of the acceleration force becomes weak. The operating temperatures are 45.7 °C, 40.6 °C, 36.0 °C, 33.3 °C, 33.1 °C and 34.1 °C at 0g, 3g, 5g, 7g, 9g and 11g, respectively.

As can be seen in Fig. 14(b), the thermal conductance shows an obvious increase with the increase of the acceleration magnitude under configuration C. In accord with the operating temperature change, thermal conductance at large heat load is also larger than that at small heat load under acceleration conditions. When the acceleration magnitude is below 7 g at 200 W, the range of the thermal conductance is from 8.5 W/K to 16.0 W/K. As the acceleration magnitude is above 7 g, the thermal conductance ranges from 20.9 W/K to 22.9 W/K. The DCCLHP operates at CCM when coupled with RTD 9 and RTD10 temperatures. However, when the heat load is 80 W, the thermal conductance ranges from 10.3 W/K to 19.8 W/K under the range of acceleration magnitude from 3 g to 11 g. it operates at VCM at 3 g whereas at CCM under 5 g and 11 g conditions.

Based on above describes, the DCCLHP could start up under different acceleration magnitude and direction conditions. The operating temperature is susceptible to the acceleration magnitude at large heat load and shows a general trend of decrease with the increase of the acceleration magnitude at small heat load. Under configuration B the loop appeared temperature oscillations and operates at a quasi-steady state as the heat load is 250 W and 300 W. The acceleration magnitude could impact on the amplitude and period of the oscillation. Furthermore, it could change the operating mode of the loop.

5. Conclusions

Experimental studies were conducted to investigate the startup behavior and operating characteristics of a DCCLHP with insufficient fluid inventory. The impact of the various control parameters such as heat load, acceleration magnitude and acceleration direction was analyzed in a systematic manner. Major findings based on the experimental results were as follows:

- (1) The DCCLHP can start up at the small heat load of 25 W under acceleration conditions.

It started up within a very short time at large heat load. Even at a fixed heat load, the DCCLHP can have a different startup behavior as it was subjected to different direction acceleration force, owing to the different vapor-liquid distribution in the evaporator and CCs.

(2) In general, the operating temperature was higher in terrestrial gravity than that under acceleration conditions. The impact of acceleration direction and magnitude on the operating temperature was significant at small heat load (≤ 150 W). But it was weak at large heat load. The acceleration force effect can change the heat load range of VCM or CCM.

(3) As the acceleration force contributed to the liquid returning back to the CCs, like under configuration C, the acceleration force effect was similar to the gravity-assisted effect. At small heat load, the entire loop temperatures had an approximate 1.0°C difference and the operating temperature was small.

(4) A number of temperature oscillation, reverse flow and evaporation in the evaporator core phenomena were observed under acceleration conditions. Especially under configuration B, it was at 250 W and 300 W that periodic temperature oscillations occurred on almost the whole loop for different acceleration magnitudes.

Acknowledgement

The authors acknowledge the financial supports from the Fundamental Research Funds for the Central Universities of China (YWF-14-HKXY-019) and the National Natural Science Foundation of China (No.51406009) as well as research funding from University of Hertfordshire.

References

- [1] X. Chen, H. Ye, X. Fan, et al., A review of small heat pipes for electronics, *Applied Thermal Engineering* 96 (2016) 1-17.
- [2] A. Faghri, Review and advances in heat pipe science and technology, *Journal of Heat Transfer* 134 (12) (2012) 123001-123019.
- [3] Y. F. Maydanik, Loop heat pipes, *Applied Thermal Engineering* 25 (2005) 635-657.
- [4] A. Ambirajan, A. A. Adoni, J. S. Vaidya, *et al.*, Loop heat pipes: A review of fundamentals, operation, and design, *Heat Transfer Engineering* 33 (4-5) (2012) 387-405
- [5] B. Siedel, V. Sartre, F. Lefèvre, Literature review: Steady-state modelling of loop heat pipes,

- Applied Thermal Engineering 75 (2015) 709-723.
- [6] J. Ku, Operating characteristics of loop heat pipes, SAE Paper No.1999-01-2007, 1999.
- [7] T. Tharayil, L. G. Asirvatham, V. Ravindran, et al., Thermal performance of miniature loop heat pipe with grapheme-water nanofluid, International Journal of Heat and Mass Transfer, 93 (2016): 957-968.
- [8] M. A. Chernysheva and Yu. F. Maydanik, Effect of liquid filtration in a wick on thermal processes in a flat disk-shaped evaporator of a loop heat pipe, International Journal of Heat and Mass Transfer, 106 (2017): 222-231.
- [9] J. He, J. Y. Miao, L. Z. Bai, et al., Effect of non-condensable gas on the startup of a loop heat pipe, Applied Thermal Engineering, 111(25) (2017) 1507-1516.
- [10] V. S. Jasvanth, A. A. Adoni, V. Jaikumar, et al., Design and testing of an ammonia loop heat pipe, Applied Thermal Engineering, 111(25) (2017) 1655-1663.
- [11] H. X. Zhang, G. P. Lin, T. Ding, et al., Investigation on startup behaviors of a loop heat pipe, Journal of Thermophysics and Heat Transfer, 19 (4) (2005) 509-518.
- [12] Y. Chen, M. Groll, R. Mertz, et al., Steady-state and transient performance of a miniature loop heat pipe, International Journal of Thermal Sciences, 45 (11) (2006) 1084-1090.
- [13] C. Gerhart and D. F. Gluck, Summary of operating characteristics of a dual compensation chamber loop heat pipe in gravity, In: Proceeding of the 11th International Heat Pipe Conference, Tokyo, Japan, 1999, pp. 67-68.
- [14] D. F. Gluck, C. Gerhart, S. Stanley, Characterization of a high capacity, dual compensation chamber loop heat pipe, American Institute of Physics Conference Proceedings, 458(1) (1999) 943-948.
- [15] D. A. Wolf and W. B. Bienert, Investigation of temperature control characteristics of loop heat pipe, SAE Paper No.941576, 1994.
- [16] J. B. Long and J. M. Ochterbeck, Transient/cyclic heat loads for dual compensation chamber loop heat pipes, Proceedings of XIIHPC, Japan Association for Heat Pipes, Tokyo, Japan, 1999, pp. 305-310.
- [17] G. P. Lin, H. X. Zhang, X. G. Shao, et al., Development and test results of a dual compensation chamber loop heat pipe, Journal of Thermophysics and Heat Transfer, 20 (4) (2006) 825-834.

- [18] L.Z. Bai, G. P. Lin, D. S. Wen, et al., Experimental investigation of startup behaviors of a dual compensation chamber loop heat pipe with insufficient fluid inventory, *Applied Thermal Engineering*, 29 (8) (2009) 1447-1456.
- [19] G. P. Lin, N. Li, L. Z. Bai, et al, Experimental investigation of a dual compensation chamber loop heat pipe, *International Journal of Heat and Mass Transfer*, 53(2010) 3231-3240.
- [20] Y. Zhao, S. Chang, B. Yang, et al., Experimental study on the thermal performance of loop heat pipe for the aircraft anti-icing system, *International Journal of Heat and Mass Transfer*, 111 (2017) 795-803.
- [21] J. Ku, L. Ottenstein, T. Kaya, et al., Testing of a loop heat pipe subjected to variable accelerating forces, part 1: start-up, SAE Paper No. 2000-01-2488, 2000.
- [22] J. Ku, L. Ottenstein, T. Kaya, et al., Testing of a loop heat pipe subjected to variable accelerating forces, part2: temperature stability, SAE Paper No. 2000-01-2489, 2000.
- [23] A. J. Fleming, S. K. Thomas, K. L. Yerkes, et al., Titanium-water loop heat pipe operating characteristics under standard and elevated acceleration fields, *Journal of Thermophysics and Heat Transfer*, 24 (1) (2010) 184-198.
- [24] K. L. Yerkes, J. D. Scofield, D. L. Courson, et al., Steady-periodic acceleration effects on the performance of a loop heat pipe, *Journal of Thermophysics and Heat Transfer*, 28 (3) (2014) 440-454.
- [25] K. L. Yerkes, J. D. Scofield, D. L. Courson, Performance of a loop heat pipe subjected to a phase-coupled heat input to an acceleration field, In: the 46th AIAA Thermophysics Conference, AIAA paper No. 2016-4145, 2016.
- [26] Y. Q. Xie, J. Zhang, L. Y. Xie, et al., Experimental investigation on the operating characteristics of a dual compensation chamber loop heat pipe subjected to acceleration field, *Applied Thermal Engineering*, 81 (2015) 297-312.
- [27] J. Z. Yu, Principle and design of heat exchanger, first edition, Beihang University Publication, Beijing, 2006, p. 239.
- [28] Moffat R J, Describing the uncertainties in experimental results, *Experimental thermal and fluid science*, 1988, 1(1): 3-17.

- Fig. 1. The schematic diagram of the experimental system.
- Fig. 2. A photo of the centrifuge and the test section enclosure.
- Fig. 3. A picture of the experimental DCCLHP and detailed construction of evaporator and CCs. (a) the DCCLHP (b) detailed construction of evaporator and CCs
- Fig. 4. Schematic of the DCCLHP and RTDs locations.
- Fig. 5. Three different directions of the acceleration. (a) Configuration A (b) Configuration B (c) Configuration C
- Fig. 6. The loop temperature profiles at 5g and 25 W under configuration A, B and C. (a) Configuration A (b) Configuration B (c) Configuration C.
- Fig. 7. Vapor-liquid distribution in the loop under configuration A, B and C. (a) Configuration A (b) Configuration B (c) Configuration C.
- Fig. 8. The loop temperature profiles at 250 W and 5 g under configuration A, B and C. (a) Configuration A (b) Configuration B (c) Configuration C.
- Fig. 9. The operating temperature and thermal conductance at 5g under three configurations and terrestrial gravity. (a) Temperature (b) Thermal conductance.
- Fig. 10. The loop temperature profiles at 80 W under terrestrial gravity and under configuration A at 5 g. (a) Terrestrial gravity (b) Configuration A at 5 g.
- Fig. 11. The loop temperature evolutions at 300 W and 3 g, 5 g, 7 g and 9 g under configuration B.
- Fig. 12. The operating temperature and thermal conductance at 150 W, 250 W and 300 W under acceleration conditions for configuration B. (a) Temperature (b) Thermal conductance.
- Fig. 13. The loop temperature evolutions at 80 W and 3 g, 5 g, 7 g, 9 g and 11 g under configuration C.
- Fig. 14. The operating temperature and thermal conductance at 80 W and 200 W under acceleration conditions for configuration C. (a) Temperature (b) Thermal conductance.
- Table 1. Major design parameters of the experimental DCCLHP

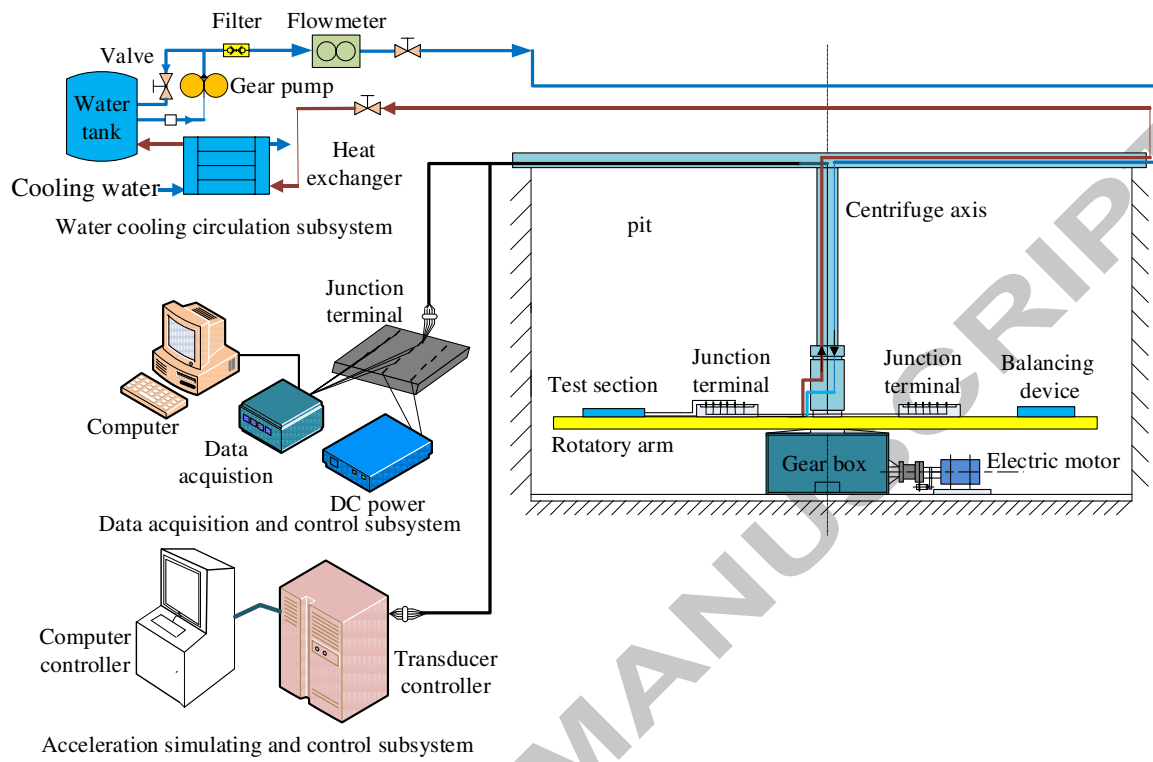


Fig. 1. The schematic diagram of the experimental system.

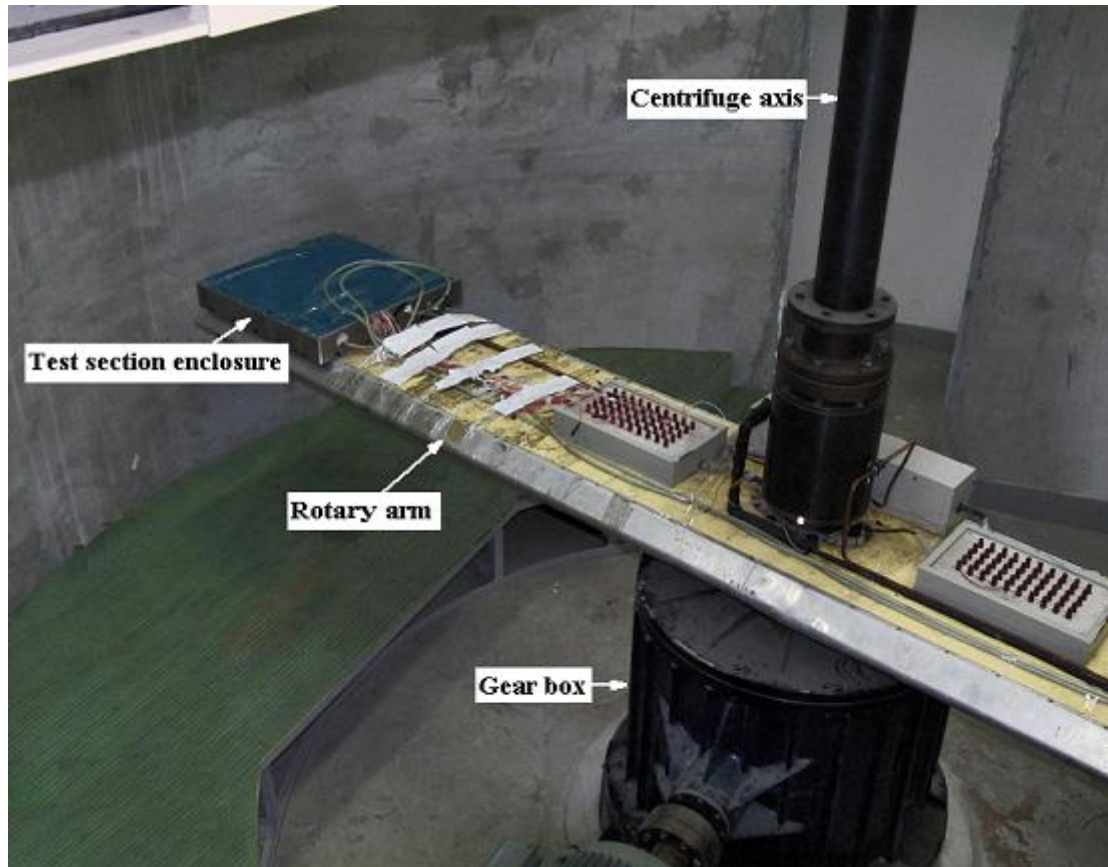
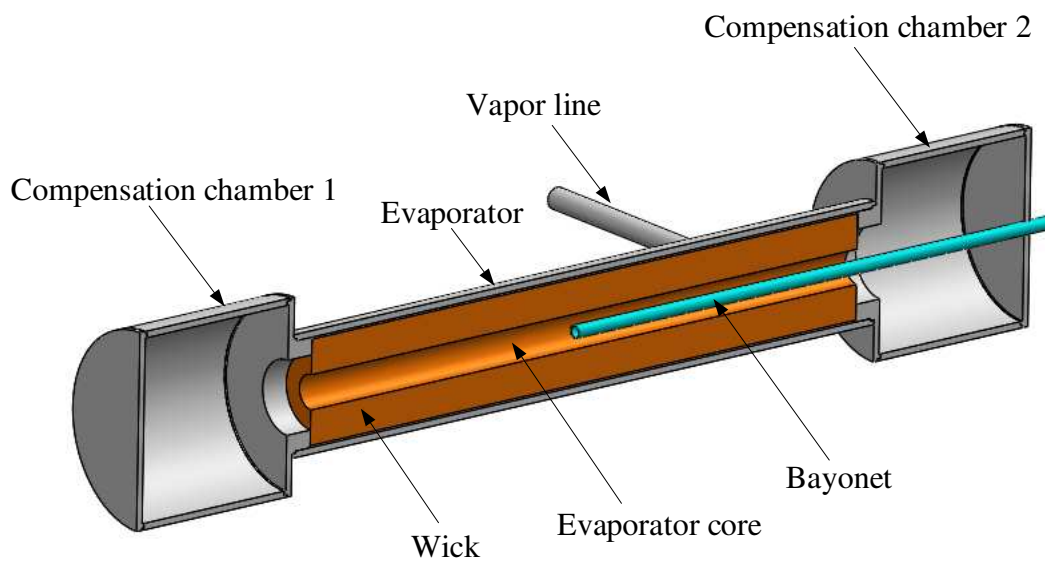


Fig.2. A photo of the centrifuge and the test section enclosure.



(a)



(b)

Fig.3. A picture of the experimental DCCLHP and detailed construction of evaporator and CCs. (a) the DCCLHP (b) detailed construction of evaporator and CCs.

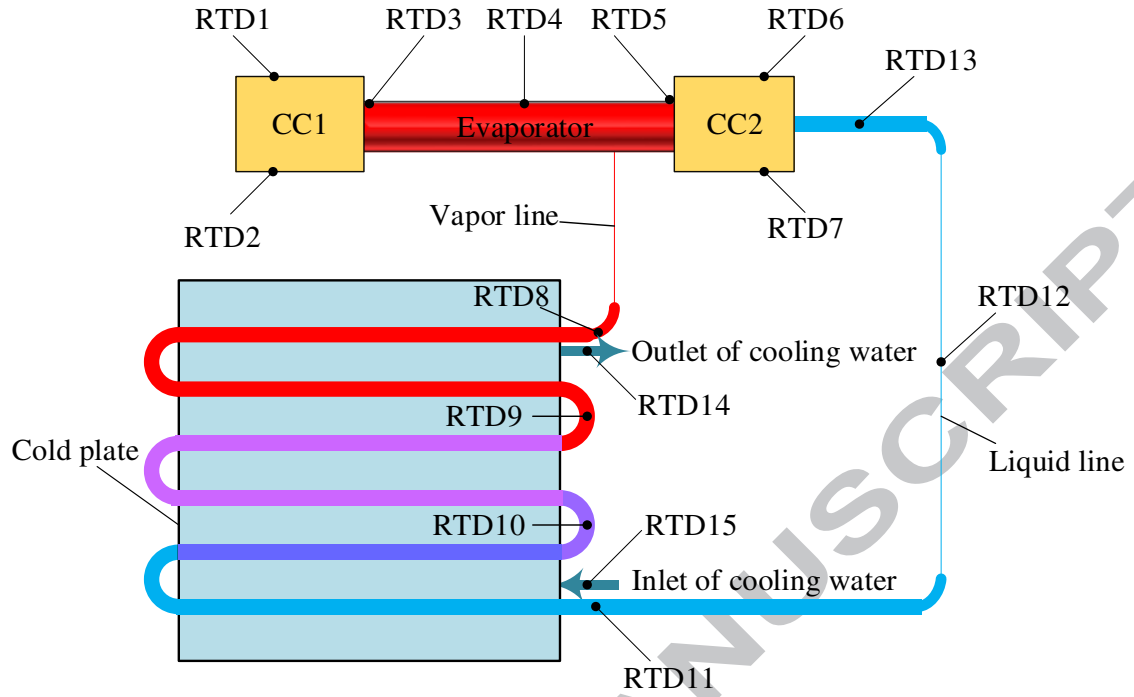
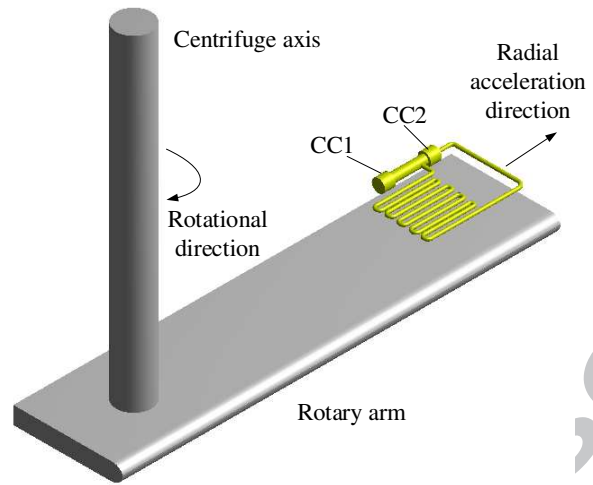
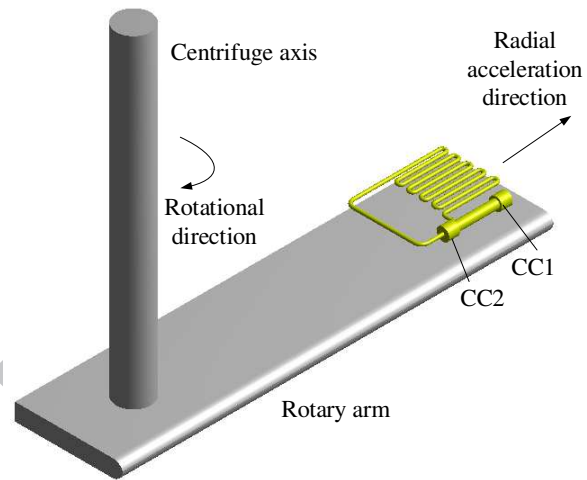


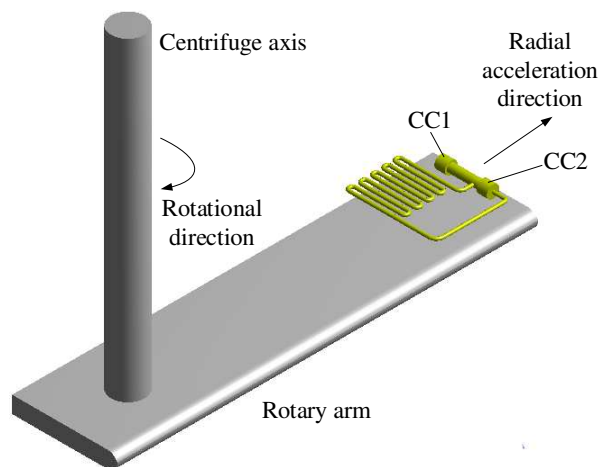
Fig.4. Schematic of the DCCLHP and RTDs locations.



(a)



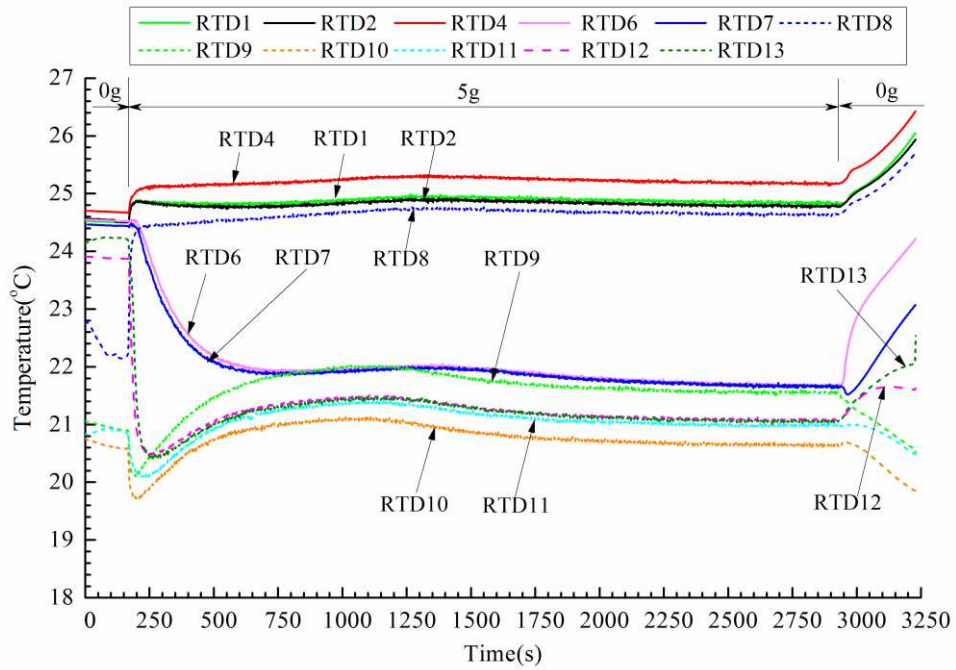
(b)



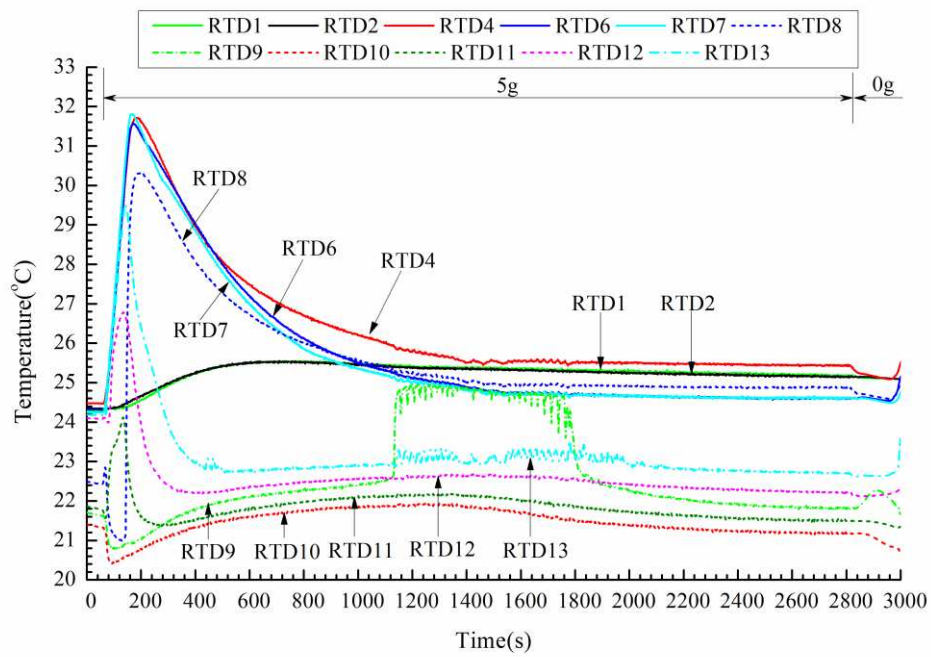
(c)

Fig.5. Three different directions of the acceleration. (a) Configuration A (b) Configuration

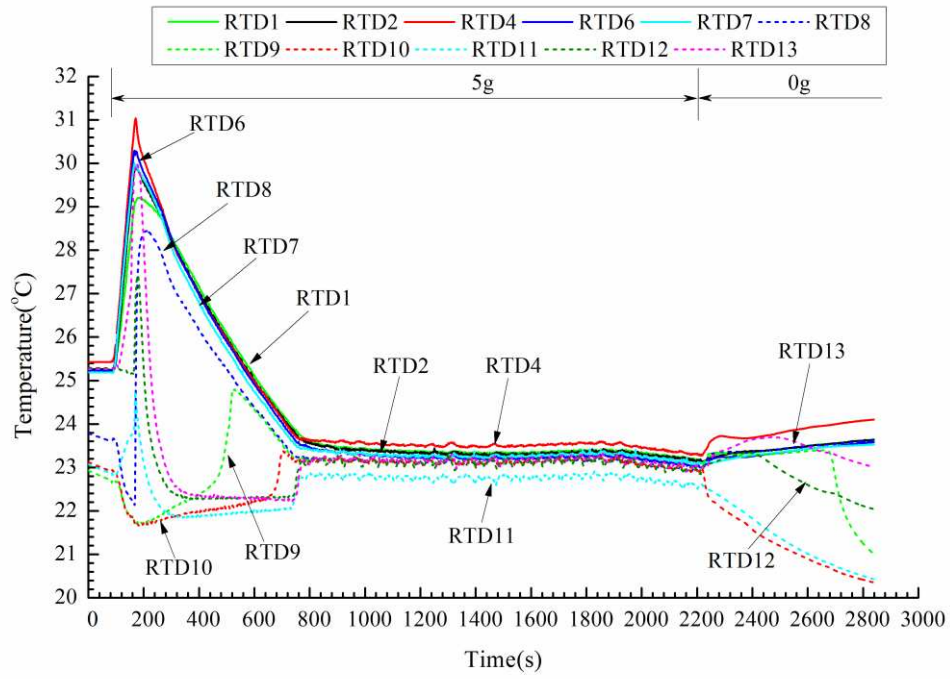
B (c) Configuration C



(a)

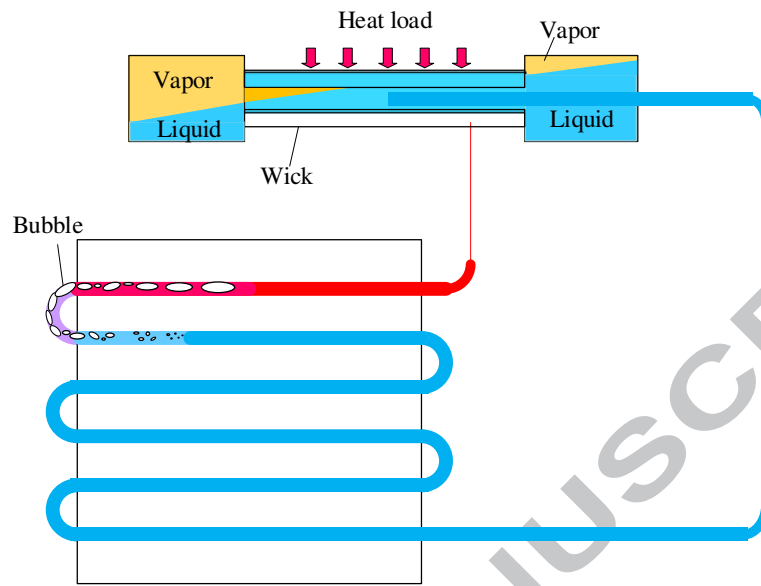


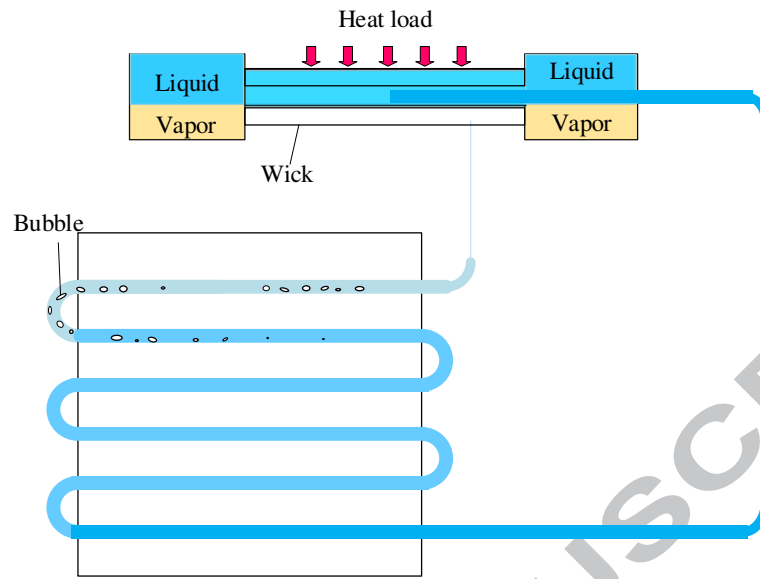
(b)



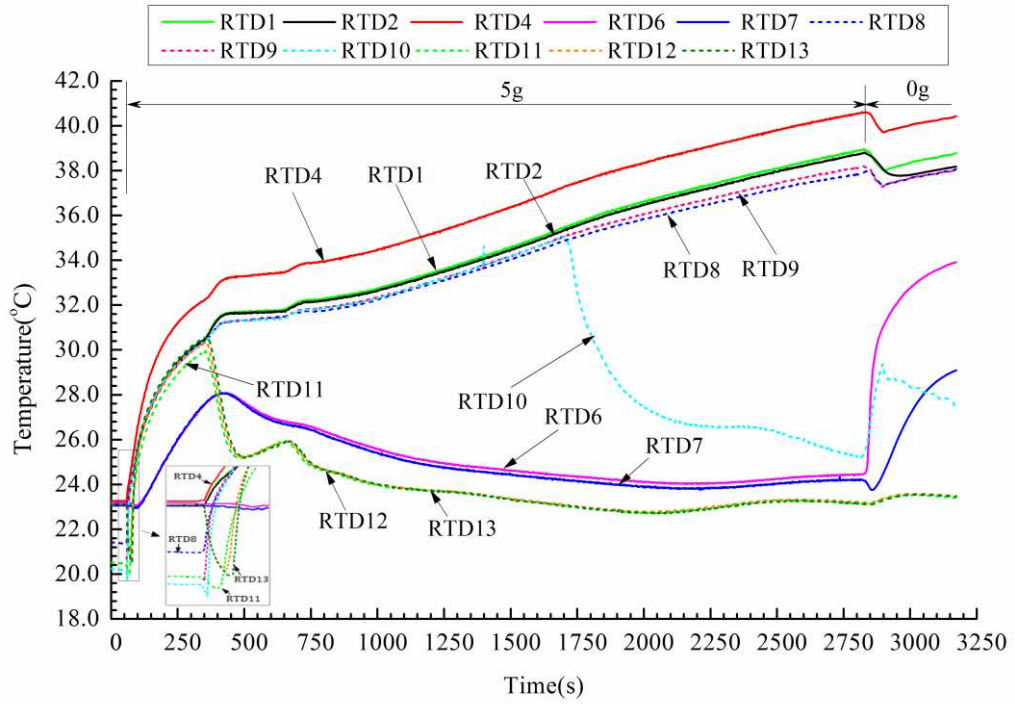
(c)

Fig. 6. The loop temperature profiles at 5 g and 25 W under three configurations. (a) Configuration A (b) Configuration B (c) Configuration C.

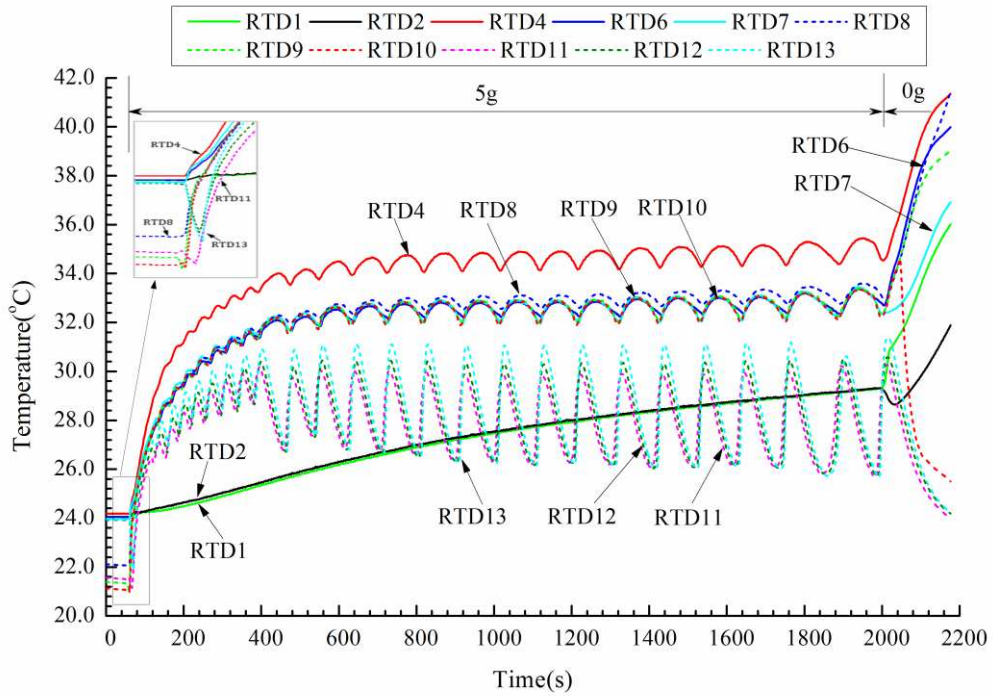




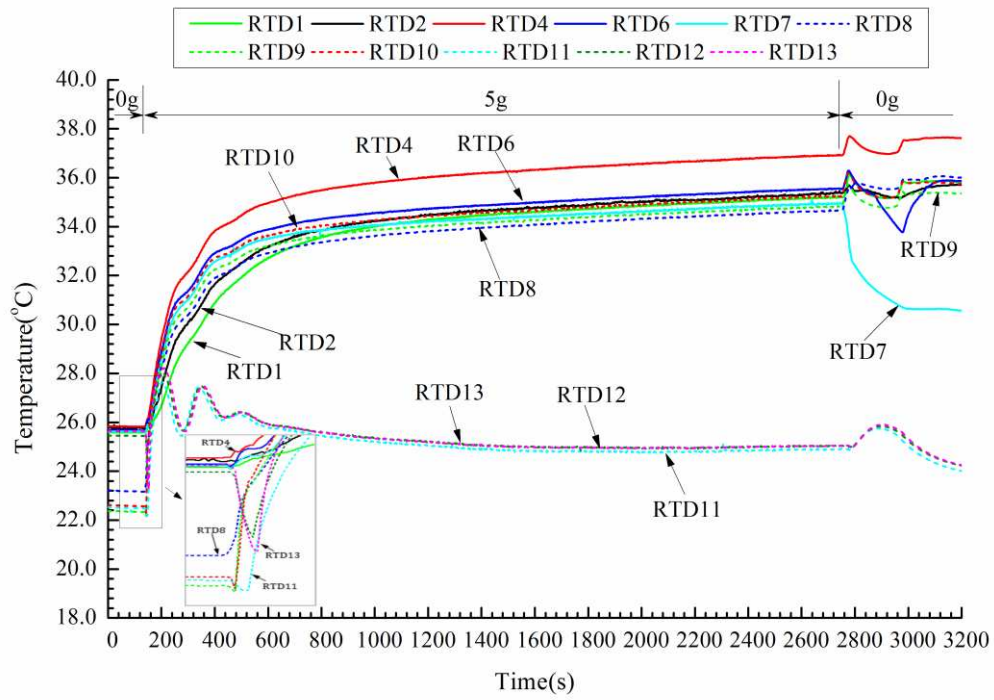
ACCEPTED MANUSCRIPT



(a)



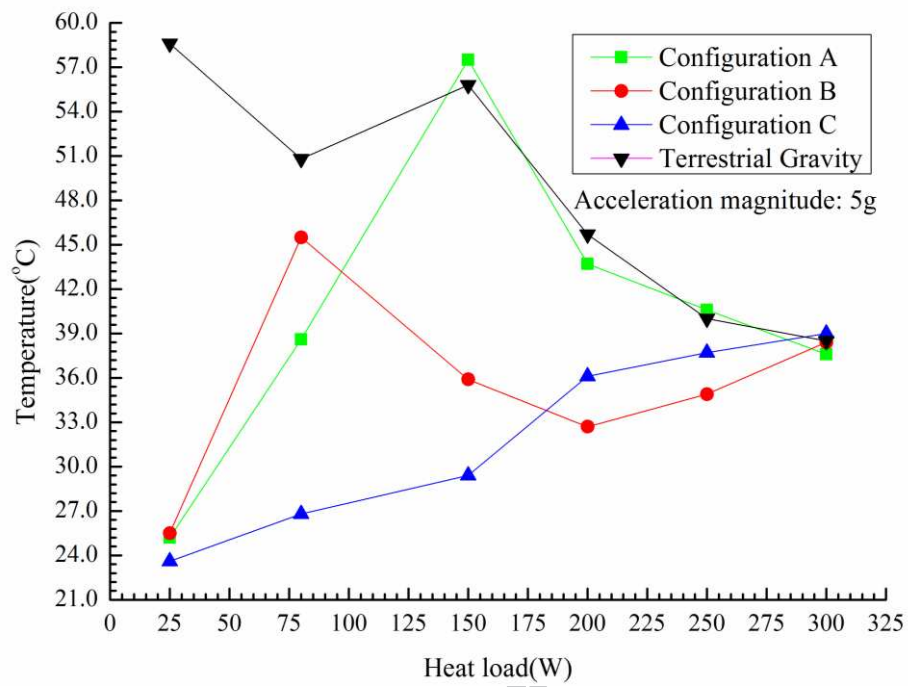
(b)



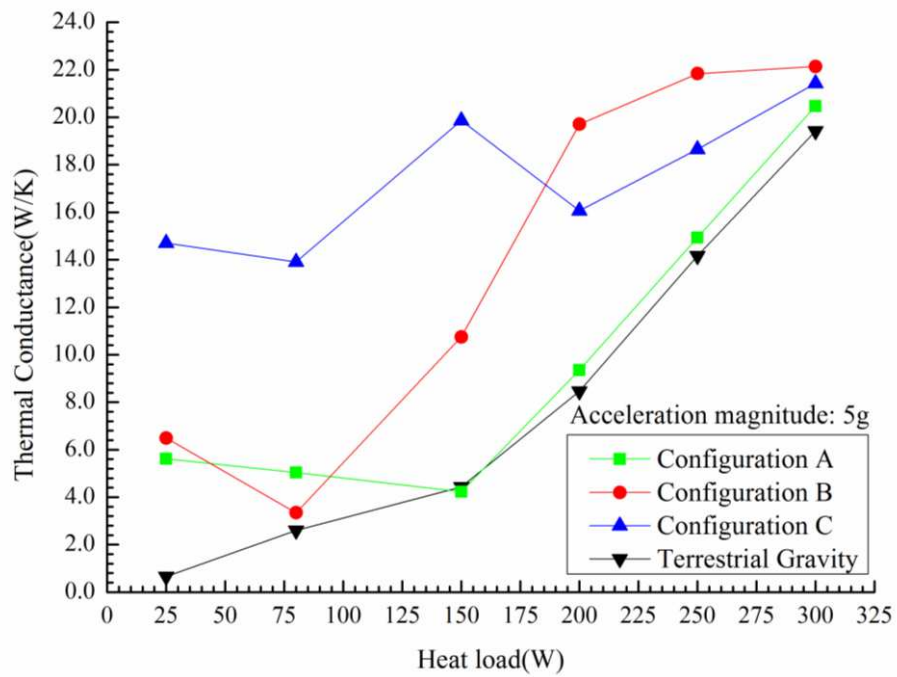
(c)

Fig. 8 The loop temperature profiles at 250 W and 5 g under configuration A, B and C. (a)

Configuration A (b) Configuration B (c) Configuration C.

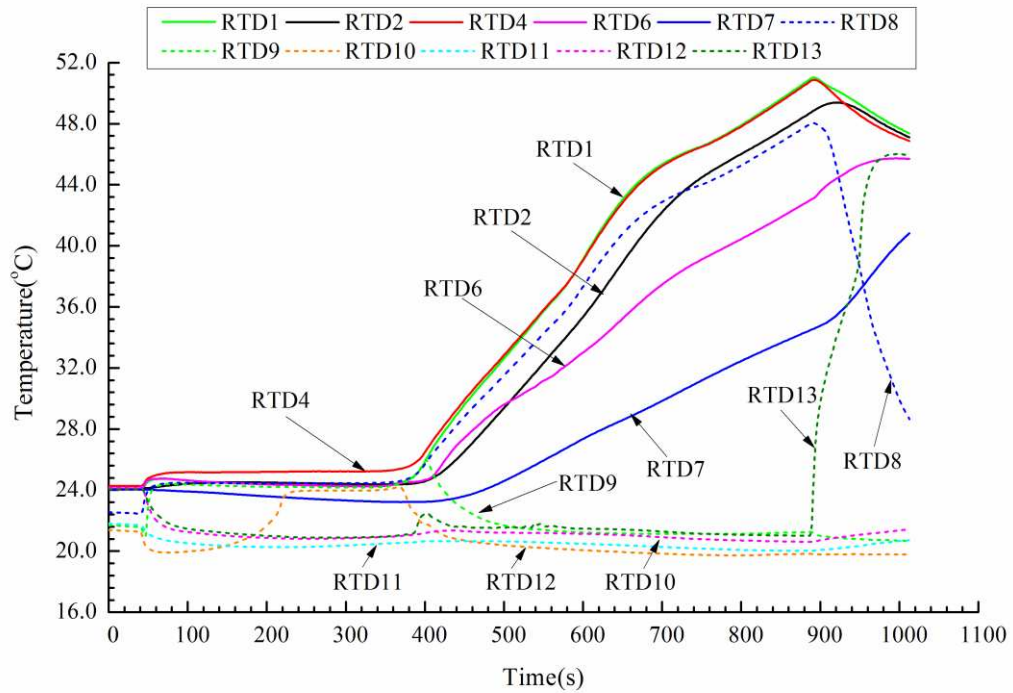


(a)

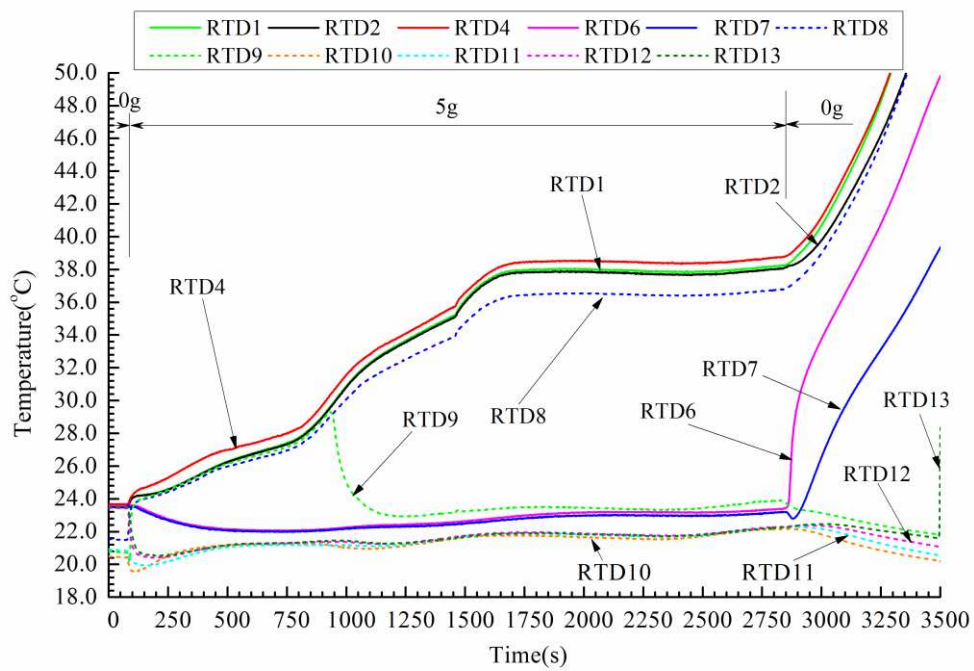


(b)

Fig.9. The operating temperature and thermal conductance at 5 g under three configurations and terrestrial gravity. (a) Temperature (b) Thermal conductance.



(a)



(b)

Fig.10 The loop temperature profiles at 80 W under terrestrial gravity and under configuration A at 5 g. (a) Terrestrial gravity (b) Configuration A at 5 g.

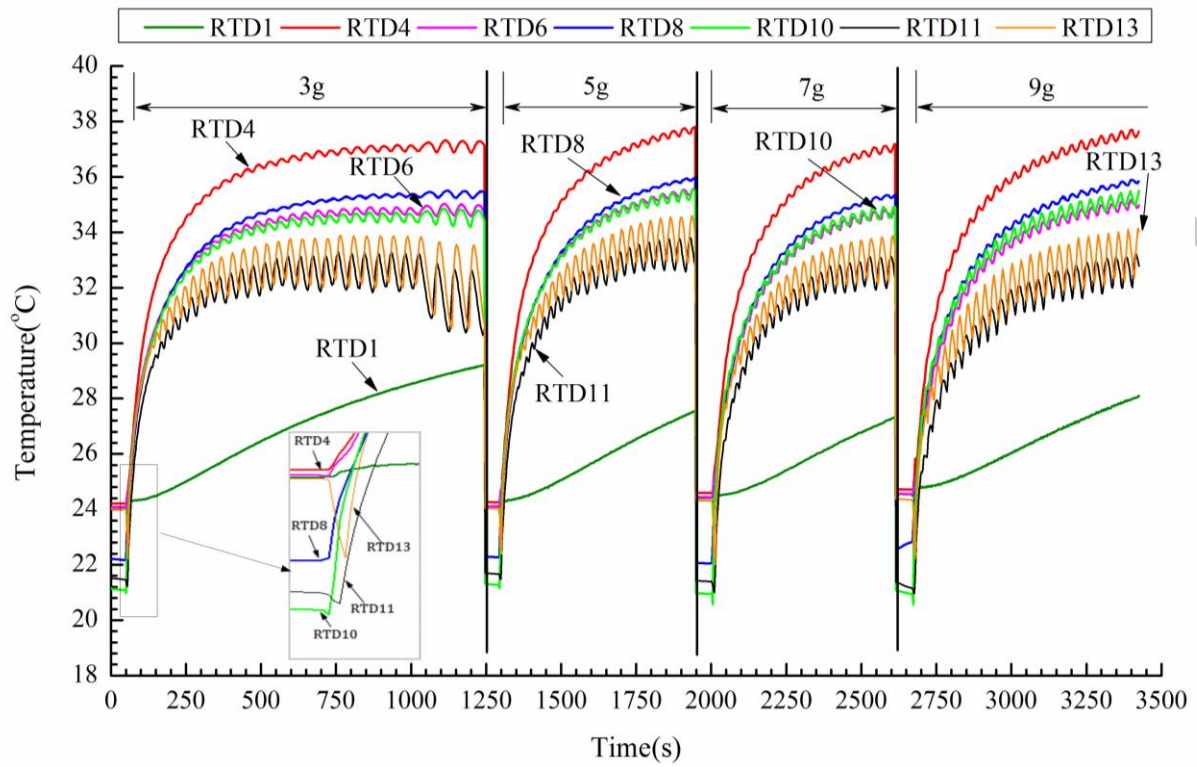
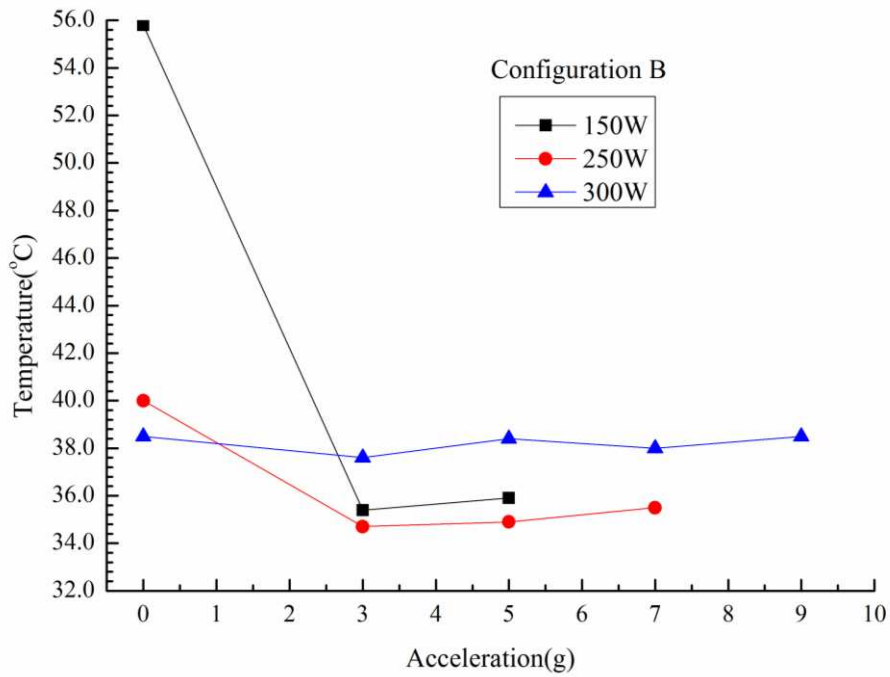
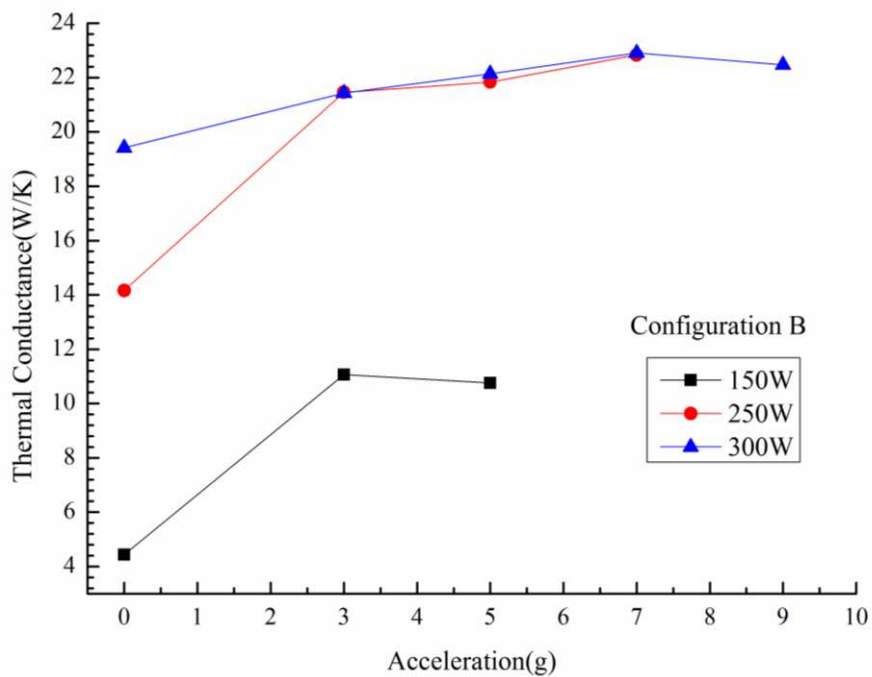


Fig.11. The loop temperature evolutions with different acceleration magnitude at 300 W for configuration B.



(a)



(b)

Fig.12. The operating temperature and thermal conductance at 150 W, 250 W and 300 W under acceleration conditions for configuration B. (a) Temperature (b) Thermal conductance.

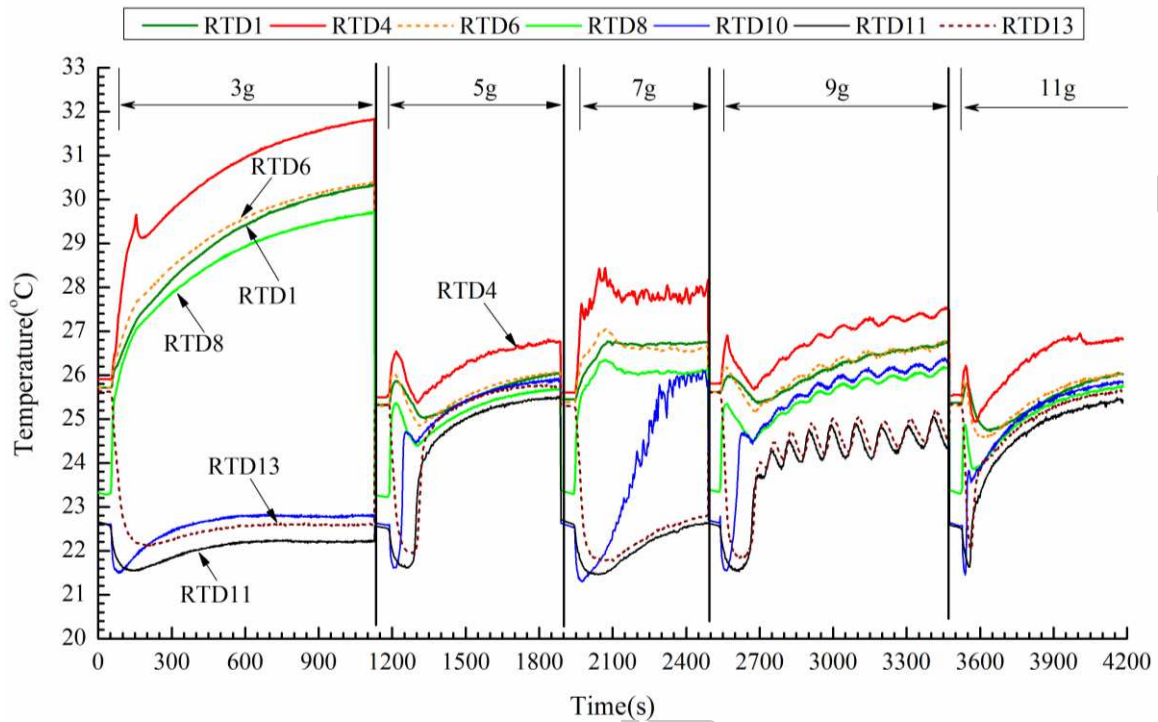
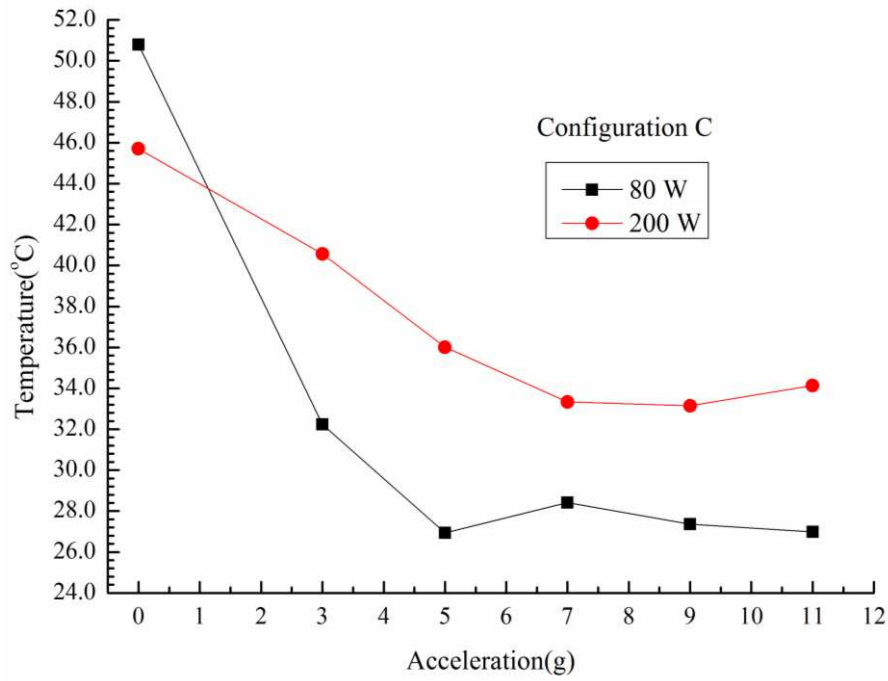
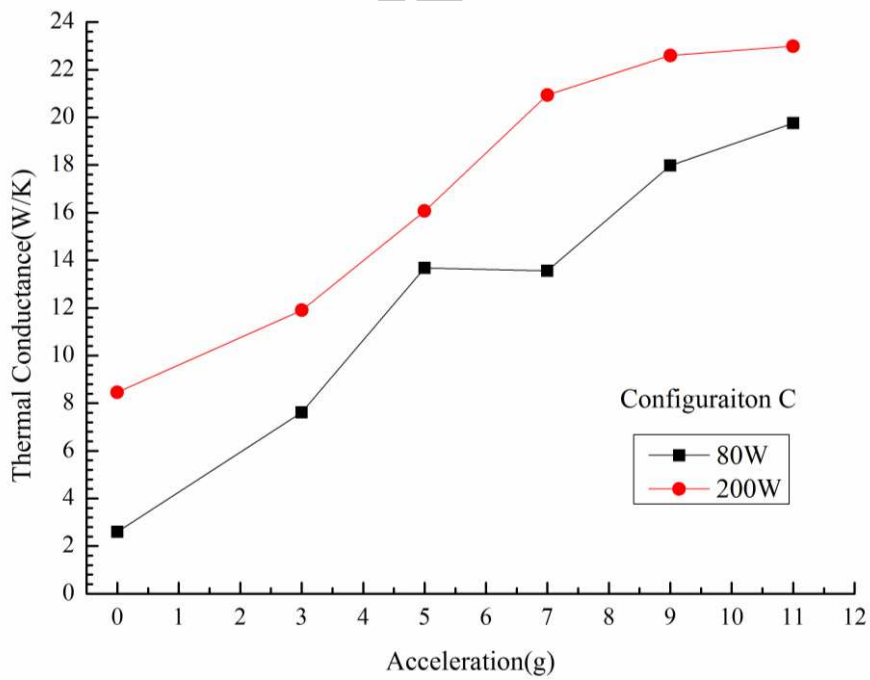


Fig.13. The loop temperature evolutions with different acceleration magnitude at 80 W for configuration C.



(a)



(b)

Fig.14. The operating temperature and thermal conductance at 80 W and 200 W under acceleration conditions for configuration C. (a) Temperature (b) Thermal conductance.

Evaporator	O.d./i.d.×length of casing	20 mm/18 mm×209 mm
	Material	Stainless steel
(primary) Wick	Pore radius	1.5 μm
	Porosity	$>5 \times 10^{-14} \text{ m}^2$
	O.d./i.d.×length	18 mm/6 mm×190 mm
	Material	Nickel
Vapor line	O.d./i.d.×length	3 mm/2.6 mm×225 mm
	Material	Stainless steel
Liquid line	O.d./i.d.×length	3 mm/2.6 mm×650 mm
	Material	Stainless steel
Condenser line	O.d./i.d.×length	3 mm/2.6 mm×2200 mm
	Material	Stainless steel
Compensation chamber	O.d./i.d.×length	27 mm/25 mm×64 mm
	Material	Stainless steel
	Number	2
Working fluid	Ammonia	

Table 1 Major design parameters of the experimental DCCLHP

Research Highlights:

- The DCCLHP transient performance is studied experimentally in acceleration field.
- Acceleration effect significantly impacts the startup behavior at small heat load.
- Acceleration effect can change the operating mode and relevant heat load range.
- Temperature oscillation and reverse flow phenomena are observed in the experiment.

ACCEPTED MANUSCRIPT